Astronomy & Astrophysics manuscript no. main
February 2, 2023

Absolute Ca II H & K and H-alpha flux measurements of low-mass stars: Extending $R'_{\rm HK}$ to M dwarfs

C. J. Marvin[1], A. Reiners[1], G. Anglada-Escudé[1,2,3], S. V. Jeffers[5], and S. Boro Saikia[1,4]

[1] Universität Göttingen, Institut für Astrophysik und Geophysik, Friedrich-Hund-Platz 1, 37077 Göttingen, Germany
[2] School of Physics and Astronomy, Queen Mary, University of London, 327 Mile End Rd. London, United Kingdom
[3] Instituto de Astrofísica de Andalucía, Glorieta de la Astronomía 1, E-18008 Granada, Spain
[4] University of Vienna, Department of Astrophysics, Türkenschanzstrasse 17, 1180 Vienna, Austria
[5] Max-Planck-Institut für Sonnensystemforschung, Justus-von-Liebig-Weg-3, 37077 Goettingen

February 2, 2023

ABSTRACT

Context. With the recent surge of planetary surveys focusing on detecting Earth-mass planets around M dwarfs, it is becoming more important to understand chromospheric activity in M dwarfs. Stellar chromospheric calcium emission is typically measured using the $R'_{\rm HK}$ calibrations of Noyes et al. (1984), which are only valid for $0.44 \leq B-V \leq 0.82$. Measurements of calcium emission for cooler dwarfs $B-V \geq 0.82$ are difficult because of their intrinsic dimness in the blue end of the visible spectrum.
Aims. We measure the absolute Ca II H & K and Hα flux of a sample of 110 HARPS M dwarfs and also extend the calibration of $R'_{\rm HK}$ to the M dwarf regime using PHOENIX stellar atmosphere models.
Methods. We normalized a template spectrum with a high signal-to-noise ratio that was obtained by coadding multiple spectra of the same star to a PHOENIX stellar atmosphere model to measure the chromospheric Ca II H & K and Hα flux in physical units. We used three different $T_{\rm eff}$ calibrations and investigated their effect on Ca II H & K and Hα activity measurements. We performed conversions of the Mount Wilson S index to $R'_{\rm HK}$ as a function of effective temperature for the range 2300 K $\leq T_{\rm eff} \leq$ 7200 K. Last, we calculated continuum luminosity χ values for Ca II H & K and Hα in the same manner as West & Hawley (2008) for $-1.0 \leq$ [Fe/H] $\leq +1.0$ in steps of Δ[Fe/H] = 0.5.
Results. We compare different $T_{\rm eff}$ calibrations and find $\Delta T_{\rm eff} \sim$ several 100 K for mid- to late-M dwarfs. Using these different $T_{\rm eff}$ calibrations, we establish a catalog of $\log R'_{\rm HK}$ and $\mathcal{F}'_{\rm H\alpha}/\mathcal{F}_{\rm bol}$ measurements for 110 HARPS M dwarfs. The difference between our results and the calibrations of Noyes et al. (1984) is $\Delta \log R'_{\rm HK} = 0.01$ dex for a Sun-like star. Our χ values agree well with those of West & Hawley (2008). We confirm that the lower boundary of chromospheric Ca II H and K activity does not increase toward later-M dwarfs: it either stays constant or decreases, depending on the $T_{\rm eff}$ calibration used. We also confirm that for Hα, the lower boundary of chromospheric flux is in absorption for earlier -M dwarfs and fills into the continuum toward later M dwarfs.
Conclusions. We confirm that we can effectively measure $R'_{\rm HK}$ in M dwarfs using template spectra with a high signal-to-noise ratio. We also conclude that our calibrations are a reliable extension of previous $R'_{\rm HK}$ calibrations, and effective temperature calibration is the main source of error in our activity measurements.

Key words. Stars: activity – Stars: chromospheres – Stars: late type

1. Introduction

M dwarfs comprise the majority of the stellar population, but their fundamental properties present challenges in measuring some of the most common activity indicators in the optical wavelength region, in particular, Ca II H and K, which lie in the bluer part of the visible spectrum. The cooler temperatures of M dwarfs imply that the bulk of their radiation lies toward longer wavelengths than for their FGK counterparts. M dwarfs are also intrinsically dimmer, which either decreases the signal-to-noise ratio (S/N) of observations or requires longer exposure times. Figure 1 demonstrates the differences in brightness and spectral energy distribution between a Sun-like G2 dwarf and a typical M4 dwarf. Additionally, telescope transmission and detector sensitivity are often higher in the redder wavelengths, which further exacerbates the problem of comparing their calcium flux with FGK stars in a consistent manner.

Send offprint requests to: C.J. Marvin, e-mail: chris.j.marvin@gmail.com

In what is known as the de facto standard of stellar activity surveys, Baliunas et al. (1995) monitored Ca II H and K lines of 111 main-sequence FGKM stars for several decades using the dimensionless measure called the Mount Wilson S index, or $S_{\rm MWO}$. This S index is a ratio of the Ca II H and K line core fluxes normalized to nearby continuum bands. However, the fluxes of the nearby continuum bands are not constant across spectral types (Vaughan & Preston 1980; Hartmann et al. 1984), which makes the comparison of stellar activity of different spectral types difficult with $S_{\rm MWO}$. To mitigate the color-dependence, $S_{\rm MWO}$ is usually transformed into a physical quantity known as $R_{\rm HK}$, which is the ratio of the Ca II H and K surface flux to bolometric flux. A more desirable measure, known as $R'_{\rm HK}$, subtracts the photospheric contribution $R_{\rm HK,\,phot}$, leaving only the chromospheric flux excess. Here, the prime denotes that the flux measurement is solely of chromospheric origin. The most common method of calculating $R'_{\rm HK}$ is the prescription derived by Noyes et al. (1984), which requires only $S_{\rm MWO}$ and $B-V$ to obtain $R'_{\rm HK}$. However, this method is only valid for $0.44 \leq B-V \leq 0.82$,

which means that M dwarfs lie outside of this $R'_{\rm HK}$ calibration range.

Despite these difficulties, measurements of Ca II H and K and Hα flux in M dwarfs have been performed before. Walkowicz & Hawley (2009) measured Ca II H and K equivalent widths for a sample of M3 dwarfs with the spectral subtraction method, using a stellar atmosphere model to correct for the photospheric flux contribution. The same technique was used by Montes et al. (1995b), who coined the term "spectral subtraction technique" and that has been performed as far back as Barden (1985) and Herbig (1985). In these studies, a synthetic spectral line profile is used as the photospheric contribution of a given star and is subtracted from an observed spectrum, resulting in a measurement of the chromospheric flux excess. Montes et al. (1995a) used the spectral subtraction technique to measure the chromospheric Ca II H and K flux excess in 28 FGK stars. Instead of using a photospheric spectrum, Cincunegui et al. (2007) measured the surface flux $F_{\rm HK}$ of main-sequence stars from early-F down to M5 spectral types, and extrapolated the Noyes et al. (1984) photospheric contribution for the M dwarfs. To measure the fractional surface flux to bolometric flux of Ca II H and K, West & Hawley (2008) used the χ method, where multiplying an equivalent width by a factor χ, a continuum measurement nearby the calcium line, results in $L_{\rm Ca\,IIHK}/L_{\rm bol}$. This study provided χ factors of Ca II H and K for the spectral range M0 - M8. However, it did not provide a correction for the photospheric contribution. To extend the photospheric flux relation down to $B - V = 1.6$ with the spectral subtraction technique, Martínez-Arnáiz et al. (2011) used a synthetic template photospheric spectrum obtained by adding together spectra of nonactive stars of similar spectral type, and measured excess surface fluxes of 298 main-sequence stars ranging from F to M. Mittag et al. (2013) used PHOENIX model atmospheres to update the relations of Noyes et al. (1984) and measured $R'_{\rm HK}$ for 2133 main-sequence stars. Instead of using stellar models, Suárez Mascareño et al. (2015) used HARPS spectra of main-sequence FGKM dwarfs to derive their own $R'_{\rm HK}$ relations down to $B - V \sim 1.9$, and measured $R'_{\rm HK}$ for 48 late-F to mid-M type stars. Scandariato et al. (2017) used the spectral subtraction technique with BT-Settl models as photospheric spectra for 71 early-M dwarfs and measured Ca II H, K, and Hα. Astudillo-Defru et al. (2017) formulated their own S-index calibration using HARPS spectra and used their own conversion from S-index to $R'_{\rm HK}$ for 403 M dwarfs. Newton et al. (2017) found $L_{\rm H\alpha}/L_{\rm bol}$ for 270 nearby M dwarfs using recomputed $\chi_{H\alpha}$ values of West & Hawley (2008).

The relation between Ca II H, K, and Hα emission (or absorption) is also of much interest. Measuring the line profiles of 147 K7-M5 main-sequence stars, Rauscher & Marcy (2006) showed that Ca II H and K lines form at slightly different heights in the chromosphere, and that the equivalent width of Hα only correlates with Ca II H and K high widths. They also reported a possible threshold above which the lower and upper chromospheres become thermally coupled. Cincunegui et al. (2007) found a clear correlation between averaged Ca II H, K, and Hα with the strongest correlation for stars with the strongest emission. Conversely, studying stars individually and at different time intervals, Cincunegui et al. (2007) found no clear indication of how Hα varies with Ca II, with stars showing correlation, anticorellation, or no correlation. Also observing individual time measurements for a sample of 30 M dwarfs, Gomes da Silva et al. (2011) found a positive correlation for the most active stars, and a tendency for a low or negative correlation in the least active stars. Walkowicz & Hawley (2009) found an initial deepening of Hα absorption for the stars that are least active in Ca II H and K before line filling and going into emission. Scandariato et al. (2017) found this same nonlinear relation between Ca II H, K, and Hα in 71 early-M dwarfs. Maldonado et al. (2017) separated older stars from younger and more active stars using the distinction of two branches identified by Martínez-Arnáiz et al. (2011). They found that the log-fluxes of Ca II H, K, and Hα relatively follow the the same linear relation for stars spectral type F to M, which they identify as being the inactive branch, and found that stars deviating from this tend to be more active and younger, and thus lie on the active branch. More recently, Reiners et al. (2022) reported relations between chromospheric Ca II H, K, and magnetic flux, and also Hα emission and magnetic flux. Combining these relations, a relation between Ca II H, K, and Hα might be derived.

Many calibrations for $R'_{\rm HK}$ exist for the main sequence from early-F to late-M spectral type. Very few studies have used high S/N coadded spectra with the spectral subtraction technique (Boro Saikia et al. (2018); Perdelwitz et al. (2021)). In fact, our work in this paper provided the M18 template-model method and measurements of Boro Saikia et al. (2018) (see Sec.2 and 3.2.2 of the aforementioned work). In this work, we measure Ca II H, K, and Hα activity with the spectral subtraction technique in a sample of 110 M dwarfs using high S/N template spectra that are flux-calibrated to PHOENIX stellar atmosphere models. The main difference of this study is that instead of taking the mean value of Ca II H and K flux measurements, we combine all available spectra and coadd them together before the flux measurement. This allows us to not just scale the Ca II H and K measurement to an absolute flux unit, but to fit the spectral energy distribution (SED) of the calcium line to a PHOENIX stellar atmosphere, and similarly for Hα. We compare three different effective temperature calibrations, and investigate their effect on Ca II H, K, and Hα activity measurements. We extend the $R'_{\rm HK}$ calibrations to 2300 K $\leq T_{\rm eff} \leq$ 7200 K using PHOENIX stellar atmosphere models. We also provide a table of $R'_{\rm HK}$ calibrations in this effective temperature range for different metallicities and surface gravities of main-sequence stars. Last, we compute the χ values of West & Hawley (2008) for Ca II H, K, and Hα for different metallicities from the PHOENIX model atmospheres.

This paper is organized as follows: In Sec. 2 we briefly review the definition of Ca II H and K and Hα activity. In Sec. 3 we discuss the sample of stars, and we calibrate $T_{\rm eff}$ using three different methods. We discuss the technique of measuring Ca II H, K, and Hα in M dwarfs with the subtraction method, using coadded template spectra and model photospheres. In Sec. 4 we discuss our Ca II H, K, and Hα measurements, provide extended $R'_{\rm HK}$ calibrations, and compare our calibrations with previous works. In Sec. 6 we summarize our work.

2. Overview of the measurement equations

2.1. Mount Wilson S-index

The HKP-2 spectrophotometer installed at the Mount Wilson Observatory measures the Ca II H and K line cores with a triangular 1.09 Å full width at half maximum (FWHM) bandpass while simultaneously measuring two 20 Å wide bands; R, centered on 4001.07 Å, and V, centered on 3901.07 Å. To mimic the response of this instrument, Duncan et al. (1991) prescribed the following S index formula:

$$S = 8\alpha \frac{N_{\rm H} + N_{\rm K}}{N_R + N_V}, \quad (1)$$

where N_H, N_K, N_R, and N_V are the counts in their respective bands, and α is a proportionality constant equating measurements made by the HKP-2 spectrophotometer to those made with HKP-1; Duncan et al. (1991) adopted the value $\alpha = 2.4$. The factor of 8 arises from the 8:1 duty cycle between the line core and continuum bandpasses. Since its inception, the S-index has been the most widely used activity indicator for FGK stars.

2.2. Chromospheric Ca II H and K ratio

To convert the dimensionless $S_{\rm MWO}$ into arbitrary surface flux $F_{\rm HK}$, Middelkoop (1982) and Rutten (1984) derived a continuum conversion factor $C_{\rm cf}$. The arbitrary surface flux is defined as

$$F_{\rm HK} = S_{\rm MWO} C_{\rm cf} T_{\rm eff}^4 10^{-14}, \quad (2)$$

and its conversion into absolute units is given by

$$\mathcal{F}_{\rm HK} = K F_{\rm HK}, \quad (3)$$

where $\mathcal{F}_{\rm HK}$ and K are in units of erg cm^{-2} s^{-1}.

$$R'_{\rm HK} = \frac{\mathcal{F}'_{\rm H} + \mathcal{F}'_{\rm K}}{\sigma T_{\rm eff}^4} = \frac{\mathcal{F}'_{\rm HK}}{\mathcal{F}_{\rm bol}}, \quad (4)$$

where $\mathcal{F}'_{\rm H} = \mathcal{F}_{\rm H} - \mathcal{F}_{\rm H,\,phot}$ and $\mathcal{F}'_{\rm K} = \mathcal{F}_{\rm K} - \mathcal{F}_{\rm K,\,phot}$. Here, $\mathcal{F}'_{\rm H}$ and $\mathcal{F}'_{\rm K}$ are the chromospheric fluxes, $\mathcal{F}_{\rm H}$ and $\mathcal{F}_{\rm K}$ are the surface fluxes, and $\mathcal{F}_{\rm H,\,phot}$ and $\mathcal{F}_{\rm K,\,phot}$ are the photospheric fluxes of the Ca II H and K lines, respectively. From a slight rearranging, Eq. 4 can be written as

$$R'_{\rm HK} = \frac{\mathcal{F}_{\rm HK} - \mathcal{F}_{\rm HK,\,phot}}{\sigma T_{\rm eff}^4} = R_{\rm HK} - R_{\rm HK,\,phot}, \quad (5)$$

with the surface flux ratio given by

$$R_{\rm HK} = \frac{\mathcal{F}_{\rm HK}}{\sigma T_{\rm eff}^4} \quad (6)$$

and the photospheric flux ratio given by

$$R_{\rm HK,\,phot} = \frac{\mathcal{F}_{\rm HK,\,phot}}{\sigma T_{\rm eff}^4}. \quad (7)$$

Typically, $R'_{\rm HK}$ is measured through a conversion from the Mount Wilson S-index. The method pioneered by Noyes et al. (1984) calculates $R_{\rm HK}$ using the equation

$$R_{\rm HK} = 1.34 \times 10^{-4} C_{\rm cf} S_{\rm MWO}. \quad (8)$$

The quantity $C_{\rm cf}$ is a color-dependent conversion factor to remove the color-dependence of the $S_{\rm MWO}$, and Noyes et al. (1984) used the Middelkoop (1982) relation,

$$\log C_{\rm cf} = 1.13(B-V)^3 - 3.91(B-V)^2 + 2.84(B-V) - 0.47, \quad (9)$$

for $0.45 \leq (B-V) \leq 1.50$. To calculate $R_{\rm phot}$, Noyes et al. (1984) used the following relation:

$$\log R_{\rm phot,\,N84} = -4.898 + 1.918(B-V)^2 - 2.893(B-V)^3 \quad (10)$$

for $0.44 \leq (B-V) \leq 0.82$. Equation 8 and Eq. 10 are then combined to obtain the chromospheric flux excess,

$$R'_{\rm HK} = R_{\rm HK} - R_{\rm phot,\,N84}. \quad (11)$$

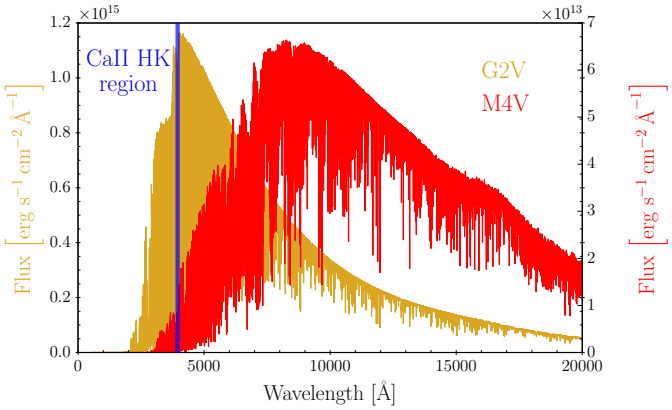

Fig. 1. Model G2V spectra (yellow) and model M4V spectra (red). The flux scale of the G2V is displayed on the left, and the flux scale of the M4V is given on the right. The blue shaded area indicates the region of the Ca II H and K lines.

2.3. H-alpha

Hα can be measured in a similar way to $R_{\rm HK}$ in Eq. 4, but substituting Hα for Ca II H and K. The chromospheric flux ratio of Hα might be defined as the surface flux subtracted by the photospheric flux, divided by the bolometric flux so that

$$\frac{\mathcal{F}'_{\rm H\alpha}}{\mathcal{F}_{\rm bol}} = \frac{\mathcal{F}_{\rm H\alpha} - \mathcal{F}_{\rm H\alpha,\,phot}}{\sigma T_{\rm eff}^4}. \quad (12)$$

In brief, we measure the surface flux of each line, $\mathcal{F}_{\rm line}$ by integrating the flux of the template spectrum, normalized to a stellar atmosphere model, inside an integration window centered on the line core. We measure the photospheric flux, $\mathcal{F}_{\rm line,\,phot}$, by integrating the flux of the stellar atmosphere model, with the same integration window centered on the line core. The bolometric flux $\mathcal{F}_{\rm bol}$ is determined from $T_{\rm eff}$, which is needed to obtain a proper stellar atmosphere model for a given star. We provide more detail in Sec. 3.

3. Case study: HARPS M dwarf sample

We used high-resolution archival spectra obtained with the HARPS spectrograph (Pepe et al. 2002) installed on ESO's 3.6m telescope in La Silla, Chile. The sample mainly consists of 102 targets from the HARPS GTO M dwarf sample (Bonfils et al. 2013)[1]. We also used data obtained for the Cool Tiny Beats survey (Anglada-Escudé et al. 2014; Berdinas et al. 2015)[2], which adds the following four stars to the sample: GJ 160.2, GJ 180, GJ 570B, and GJ 317. Last, the following six M dwarfs with published planetary systems, and that are available in the ESO HARPS public archive, were added: GJ 676A, GJ 1214, HIP 12961, GJ 163, GJ 3634, and GJ 3740. Photometry values, mean radial velocities, proper motions, and parallaxes were acquired from SIMBAD (Wenger et al. 2000) (see Table D.1).

3.1. High S/N template spectra

We used the HARPS-TERRA software (Anglada-Escudé & Butler 2012) for all available spectra on all stars in the sample. HARPS-TERRA is a sophisticated tool that matches individual

[1] ESO IDs 082.C-0718 and 183.C-0437
[2] ESO ID 191.C-0505

Table 1. PHOENIX grid parameter space

	Min	Max	Step size
$T_{\rm eff}$ [K]	2300	7200	100
[Fe/H]	-1.0	+1.0	0.5
log(g)	4.0	5.0	0.5

spectra to a high S/N "template spectrum" using a least-squares fit to compute high-precision radial velocities. The high S/N template spectrum is obtained by coadding all individual spectra of a given star using the highest S/N spectrum as a basis spectrum. Pixel weighting, telluric masking, and outlier filtering are all implemented in the algorithm to assess and reduce systematic biases (see Sec. 2 in Anglada-Escudé & Butler (2012) for a much more detailed explanation). Because of this technique, the template spectrum for a star is essentially an averaged spectrum with median clipping. For each star, we obtained a high S/N template spectrum of each spectral order. We then used the corresponding spectral order that contains the chromospheric line of interest as the stellar observation spectrum.

After the initial run of HARPS-TERRA on all spectra of each target, we ran HARPS-TERRA a second time, excluding spectra that matched any of the following criteria: 1) program ID 60.A-9036(A), where spectra were acquired under nonoptimal conditions (an engineering run), 2) spectra reduced with cross-correlation function (CCF) masks earlier than M2 (the HARPS DRS pipeline uses an M2 mask for all M stars), and 3) spectra with radial velocity (RV) outliers determined by inspection. In general, looking at the RV time-series, spurious observation differences on the order of 1-10 km/s with respect to most observations are considered outliers. All three of the above criteria could negatively influence the resulting template spectra in a suboptimal way. After the second run of HARPS-TERRA, we corrected for the blaze function by running HARPS-TERRA a third time with the `-useblaze` option and the blaze file given by the `ESO DRS BLAZE FILE` keyword in the template spectrum file header. Finally, we obtained a blaze-corrected high S/N template spectrum for each star.

3.2. Photospheric flux from stellar atmosphere models

To calculate photospheric fluxes, we used a grid of PHOENIX-ACES stellar atmosphere models from the Göttingen Spectral Library[3] (Husser et al. 2013). The parameters and step sizes of the grid are listed in Table 1. We calculated $\mathcal{F}_{\rm HK,\,phot}$ by setting a 1.09 Å FWHM triangular bandpass centered on the Ca II H and K lines and summing the flux. The triangular bandpass mimics the response of the H and K bands of the HKP-2 Mount Wilson spectrograph (Duncan et al. 1991) (see Sec. 2.1). To measure the fractional chromospheric flux $\mathcal{F}'_{\rm H\alpha}/\mathcal{F}_{\rm bol}$, we used a 5.0 Å wide rectangular bandpass centered on Hα.

3.3. Surface flux from a high S/N template spectum

For a given star, the surface flux is measured from the high S/N template spectrum computed in Sec. 3.1. In the left panel of Fig. 2, we plot a single HARPS observation of the Ca II K line of an M1.5 star. Because HARPS has a high resolution of $R \sim 110,000$, the S/N in the region near the calcium line is low, as shown in the figure. The right panel of Fig. 2 shows the same line of the same star, but this time, with 47 observations coadded together. This demonstrates the considerable S/N improvement obtained by coadding spectra.

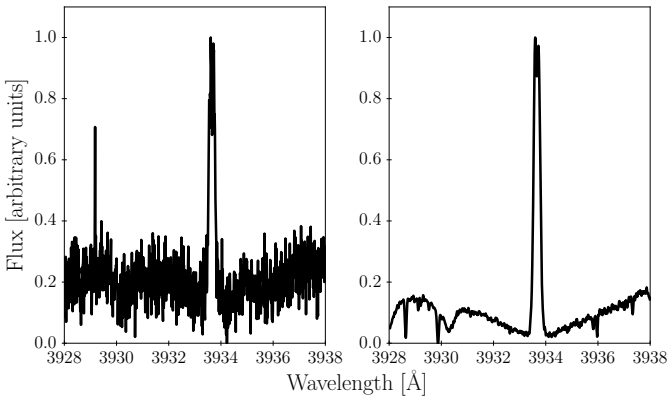

Fig. 2. Ca II K line of an M1.5 star. *Left*: Spectrum of a single HARPS observation. *Right*: Template spectrum consisting of 47 coadded spectra of the same star.

For a single chromospheric line of a given star, the entire template order spectrum is normalized to a PHOENIX model spectrum via a first-degree polynomial least-squares fit, namely $\mathcal{F}(\lambda) = af(\lambda) + b$. The PHOENIX spectra were bilinearly interpolated to a precision of $\Delta T_{\rm eff} = 1$ K and Δ[Fe/H] = 0.01 dex using the stellar parameters chosen by the methods outlined in Sec. 3.5 and listed in Table D.2. For the Ca II K line, we used order 6, for the Ca II H line, we used order 8, and for Hα, we used order 68. Before normalizing the template spectrum to the PHOENIX spectrum, we converted counts into energy, shifted the spectrum to rest wavelengths, and then transformed wavelengths to vacuum wavelengths. We masked the active lines, as well as Hϵ at 3971.2 Å. To reduce the influence of low S/N at the spectral order edges from the blaze function, we also masked the outer 10% of each order. We took the sum of the line flux in the same manner as in Sec. 3.2.

Figure 3 demonstrates this normalization of a high S/N template spectrum of an early-M dwarf normalized to a PHOENIX atmosphere model around the Ca II K line. The high S/N template spectrum consists of all available spectra coadded and flux-calibrated to the PHOENIX model atmosphere. Similarly, Fig. 4 shows this normalization of an M dwarf with Hα in absorption, while Fig. 5 shows another M dwarf with Hα in emission.

3.4. S-index comparison

As a sanity check, we compared the S -index values of our sample (for their values, we refer to Boro Saikia et al. (2018) and for the treatment of how they were calculated) with those of Astudillo-Defru et al. (2017) in Fig. 6. Although it agrees, the linear fit slightly overestimates the values of Astudillo-Defru et al. (2017) compared to Boro Saikia et al. (2018) for S values below 2,

$$S_{\rm AD17} = 1.0487 S_{\rm BS18} + 0.008 \tag{13}$$

3.5. Stellar parameters

For an accurate stellar atmosphere model to normalize a template spectrum to, we must first determine a set of stellar parameters for each star in a self-consistent manner. Here we describe the

[3] http://phoenix.astro.physik.uni-goettingen.de/

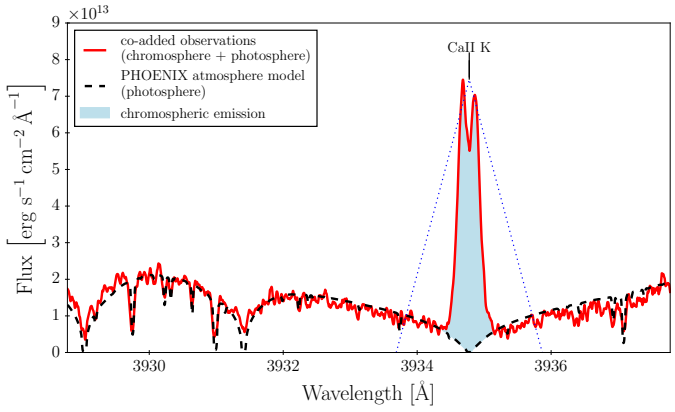

Fig. 3. High S/N template spectrum of an early-M dwarf normalized to a PHOENIX atmosphere model. The solid red line is the high S/N template spectrum, while the dashed black line is the PHOENIX model atmosphere. The blue shaded region shows the chromospheric emission. The dotted lines indicate the 1.09 Å FWHM triangular bandpass used to integrate the Ca II H and K lines.

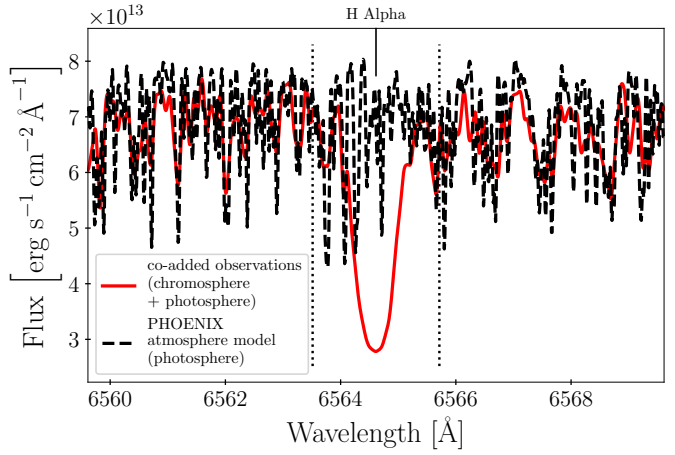

Fig. 4. High S/N template spectrum of an M dwarf with Hα in absorption normalized to a PHOENIX atmosphere model. The solid red line is the high S/N template spectrum, while the dashed black line is the PHOENIX model atmosphere. The vertical dotted lines indicate a 5.0 Å integration region.

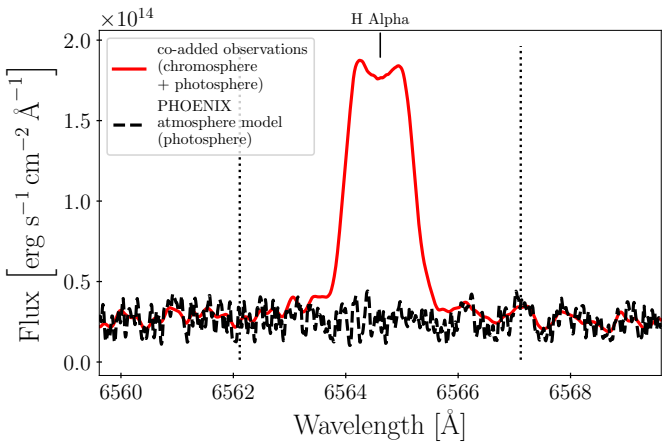

Fig. 5. High S/N template spectrum of an active M dwarf with Hα in emission normalized to a PHOENIX atmosphere model. The solid red line is the high S/N template spectrum, while the dashed black line is the PHOENIX model atmosphere. The vertical dotted lines indicate the 5.0 Å integration region of Hα.

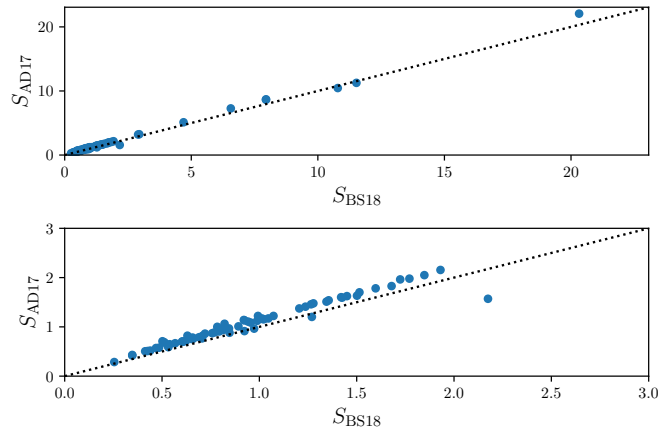

Fig. 6. $S_{\rm AD17}$ of Astudillo-Defru et al. (2017) vs our work $S_{\rm BS18}$ (Boro Saikia et al. 2018). *Top*: Entire range of the sample. *Bottom*: Same sample with zoomed in axes. The dotted line shows the 1:1 relation.

different calibrations we used to determine effective temperature and how we determined metallicity.

Effective temperature For each star in the sample, we estimated $T_{\rm eff}$ using three different calibrations. The first and second calibration used the combined relation of spectral type, effective temperature, mass, and radius from Kenyon & Hartmann (1995) and Golimowski et al. (2004). This same combination of calibrations was used by Reiners & Basri (2007), Shulyak et al. (2011), and Reiners & Mohanty (2012). The first method simply converts spectral type into effective temperature. We denote effective temperatures obtained from this method with $T_{\rm eff,SpT}$. The second method uses the M_{K_S}–$\mathcal{M}_\star$ calibration of Delfosse et al. (2000) to first obtain a mass $\mathcal{M}_\star$ from the absolute M_{K_S} magnitude, and then uses the former relation to convert $\mathcal{M}_\star$ into $T_{\rm eff}$. We denote effective temperatures obtained from this method with $T_{\rm eff,\mathcal{M}_\star}$. The third method adopts $T_{\rm eff}$ values obtained by Maldonado et al. (2015) of 53 stars in the HARPS M dwarf GTO sample. We denote effective temperatures from this study with $T_{\rm eff,M15}$.

Metallicity Maldonado et al. (2015) also calculated metallicities of the same 53 targets using the pseudo-equivalent width (PEW) technique of Neves et al. (2014), who also calculated metallicities for the entire HARPS GTO M dwarf sample. Maldonado et al. (2015) reported that their results agreed well overall with those of Neves et al. (2014), and we therefore adopted the metallicities of Neves et al. (2014) for the sample completeness. Although effective temperatures were also calculated, the authors noted that their $T_{\rm eff}$ values are systematically underestimated compared with other works; therefore, we did not adopt the $T_{\rm eff}$ values of Neves et al. (2014). For two stars not listed in Neves et al. (2014) (GJ 570B and GJ 180), we used the conversion of M_{K_S} and $V-K$ to [Fe/H] in Neves et al. (2012). We note that the difference in metallicities between Neves et al. (2012) and Maldonado et al. (2015) can be up to Δ[Fe/H] ± 0.2. However, this difference is much smaller than the resolution of our grid of models, Δ[Fe/H] ± 0.5. For stars with no M_{K_S} or $V-K_S$ measurements, we assumed solar metallicity. For all stars in the sample,

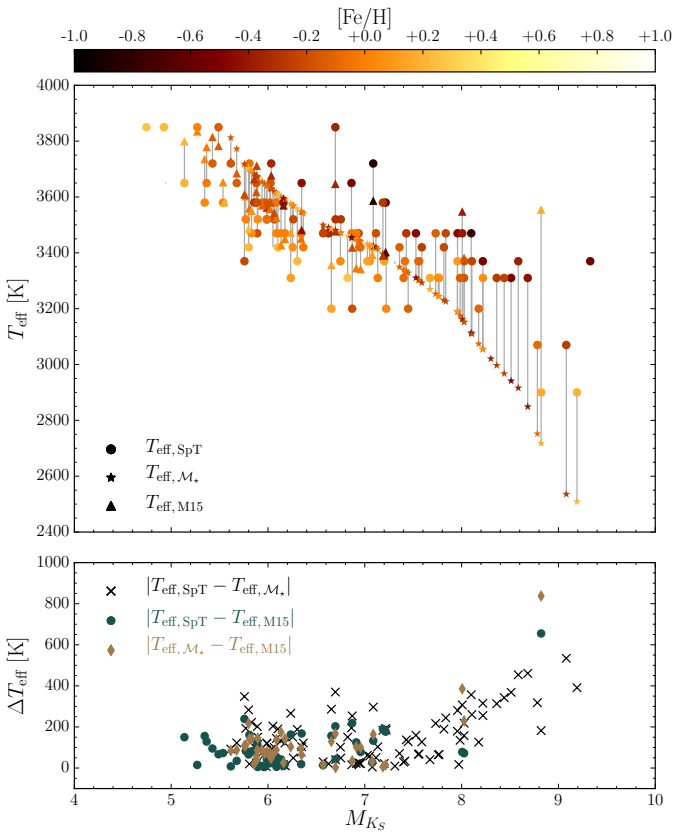

Fig. 7. Effective temperature $T_{\rm eff}$ of the stellar sample using different $T_{\rm eff}$ determination methods, which are shown by different plot symbols. *Top*: Effective temperature $T_{\rm eff}$ as a function of absolute magnitude M_{K_S} with metallicity [Fe/H] shown according to the color scale. Temperatures of the same star are connected with a solid vertical line. *Bottom*: Difference of the methods used to obtain $T_{\rm eff}$ in K.

we constrained the surface gravity to $\log(g) = 5.0$, which is a typical value for M dwarfs. The stellar parameters we used are listed in Table D.2.

The top panel of Fig. 7 shows $T_{\rm eff}$ of the three methods we used as a function of M_{K_S}, with their metallicity represented by color. For $T_{\rm eff,SpT}$, we were able to calibrate 110 stars. With $T_{\rm eff,\mathcal{M}_\star}$, we were able to calibrate 99 stars, and for $T_{\rm eff,M15}$, there are 49 stars. Temperatures of the same star are connected with a solid vertical line. In the lower panel of Fig. 7, we show the residuals of the different sources of $T_{\rm eff}$. As is evident from both panels, the $T_{\rm eff}$ determined by different methods disagrees to some extent, and this becomes much more pronounced for stars with $M_{K_S} > 8$. The mean of all $\Delta T_{\rm eff}$ values is 176 K. For $\Delta T_{\rm eff}$ values with $M_{K_S} < 8$, the mean difference drops to 122 K. The mean of $\Delta T_{\rm eff}$ values for $M_{K_S} > 8$ increases to 363 K. Most of these values with $M_{K_S} > 8$ belong to $T_{\rm eff,\mathcal{M}_\star} - T_{\rm eff,SpT}$.

We note that metallicity has an effect on the $T_{\rm eff}$ determination. The largest scatter in $\Delta T_{\rm eff}$ is between $T_{\rm eff,SpT}$ and $T_{\rm eff,M15}$. The determination of the spectral type depends on line ratios that are sensitive to both $T_{\rm eff}$ and [Fe/H]. Moreover, Maldonado et al. (2015) determined $T_{\rm eff}$ simultaneously with metallicity, However, metallicity does not have much impact when determining $T_{\rm eff}$ from M_{K_S}-$\mathcal{M}_\star$, as infrared absolute magnitudes are less sensitive to metallicity (Delfosse et al. 2000). For $T_{\rm eff,\mathcal{M}_\star}$, since $\mathcal{M}_\star$ is determined from a polynomial as a function of M_{K_S}, we expect to see a clear relation between $T_{\rm eff}$ and M_{K_S}. Whether M_{K_S} actually is such a precise indicator of $T_{\rm eff}$ is beyond the context of this study. Regardless, accurate effective temperatures of M dwarfs remain elusive; see Mann et al. (2015) and Passegger et al. (2016) for more thorough analyses of the current state of M dwarf stellar parameter determination.

4. Results

4.1. Chromospheric Ca II H and K flux

We plot the chromospheric Ca II H and K flux normalized to bolometric flux, $\log R'_{\rm HK}$, as a function of absolute magnitude M_{K_S} in Fig. 8. $\log R'_{\rm HK}$ was calculated using the spectral subtraction technique outlined in Sec. 3, following Eq. 4. We estimated $T_{\rm eff}$ using the three different methods described in Sec. 3.5 and for each $T_{\rm eff}$, calculated $\log R'_{\rm HK}$. The plot legend contains the colors of each $T_{\rm eff}$ calibration. We connect $\log R'_{\rm HK}$ measurements of the same star but different effective temperatures with a solid vertical line. Additionally, we plot stars with known planetary systems with open symbols, and stars without known planetary systems with closed symbols. Stars without Hα in emission are plotted with a circle and stars exhibiting Hα emission with a triangle.

4.1.1. $T_{\rm eff,SpT}$ calibration

For 110 stars we have spectral type information and are able to measure $\log R'_{\rm HK}$ using the spectral type to $T_{\rm eff}$ conversion, $T_{\rm eff,SpT}$. Of these stars, 13 exhibit Hα emission, and 19 have known planetary systems. The earliest-M dwarfs with $M_{K_S} < 5.8$ have higher values of $\log R'_{\rm HK}$, between -4.8 and -4.5. There is a drop in the lower boundary of activity levels near $M_{K_S} = 5.7$, where values range from $-5.3 < \log R'_{\rm HK} < -4.7$. After this drop, the sequence of lower-activity stars has no apparent drop, and $\log R'_{\rm HK}$ stays between -5.5 and -4.9. Stars exhibiting Hα emission tend to have much higher $\log R'_{\rm HK}$ values than those that do not exhibit Hα emission. Their measured activity levels are $\log R'_{\rm HK} > -4.7$ and can be as high as $\log R'_{\rm HK} = -3.8$

4.1.2. $T_{\rm eff,\mathcal{M}_\star}$ calibration

For 99 stars, we have M_{K_S} measurements and can measure $\log R'_{\rm HK}$ using the M_{K_S} to mass to $T_{\rm eff}$ calibration $T_{\rm eff,\mathcal{M}_\star}$. Of these stars, 13 exhibit Hα emission, and 16 have known planetary systems. Unlike $\log R'_{\rm HK}$ measured with $T_{\rm eff,SpT}$, the lower boundary of activity for $T_{\rm eff,\mathcal{M}_\star}$ decreases with M_{K_S}. This relation is expected because in this case, $T_{\rm eff,\mathcal{M}_\star}$ is calibrated using M_{K_S}. This does not have a dramatic effect on $\log R'_{\rm HK}$ values until $M_{K_S} = 8$. At higher M_{K_S}, the difference in $\log R'_{\rm HK}$ can be as high as 1.3 dex, and this arises from the large differences in $T_{\rm eff}$ seen in Fig. 7. However, even though the measured values of $\log R'_{\rm HK}$ using $T_{\rm eff,\mathcal{M}_\star}$ are much lower, stars with Hα in emission still have significantly higher $\log R'_{\rm HK}$ values than their counterparts.

4.1.3. $T_{\rm eff,M15}$ calibration

For 49 stars with adopted values from Maldonado et al. (2015), we are able to measure $\log R'_{\rm HK}$ using $T_{\rm eff,M15}$. Of these stars, 4 exhibit Hα emission, and 9 have known planetary systems. Similar with the other $T_{\rm eff}$ calibrations, the lower level of $\log R'_{\rm HK}$ decreases from -4.5 to -5.4 between $5 < M_{K_S} < 6.4$. There are only three stars with $M_{K_S} \gtrsim 8$, and they tend to agree more with $T_{\rm eff,SpT}$ values than $T_{\rm eff,\mathcal{M}_\star}$.

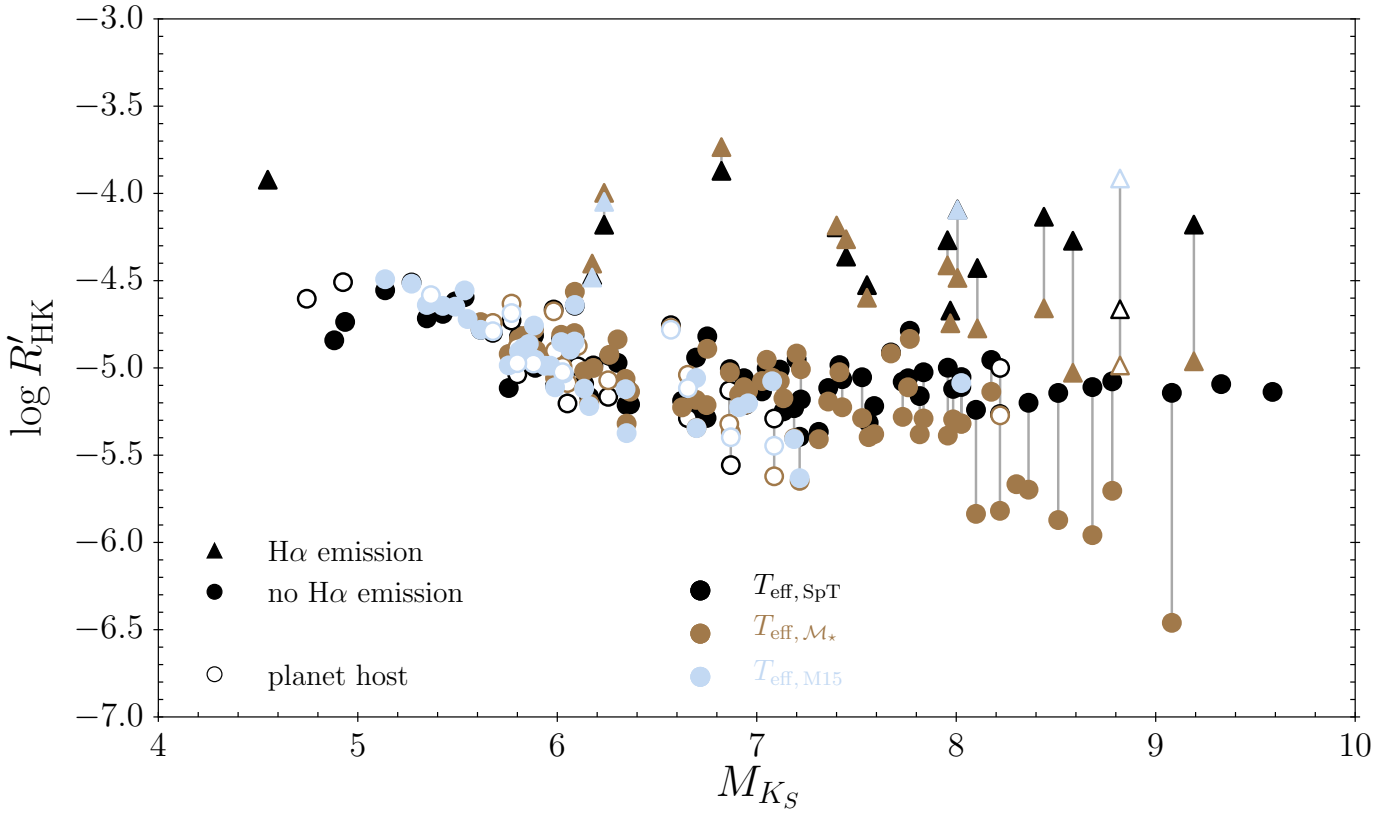

Fig. 8. Fractional chromospheric Ca II H and K flux normalized to bolometric flux on a logarithmic scale, $\log R'_{\rm HK}$, as a function of absolute magnitude M_{K_S}. For each star, $\log R'_{\rm HK}$ is calculated with different $T_{\rm eff}$ calibrations, each plotted with a different color. Vertical gray lines connect different measurements of the same star. Triangles indicate stars exhibiting Hα emission. Filled symbols indicate stars without known planetary systems, and open symbols indicate stars with known planetary systems.

We list the individual $\log R'_{\rm HK}$ measurements in Table D.3. The largest differences of $\log R'_{\rm HK}$ values occur at the latest spectral types where it is difficult to determine a consistent $T_{\rm eff}$ using a color, magnitude, or spectral type relation. For the entire sequence of stars, the mean of $\Delta \log R'_{\rm HK}$ is 0.17 dex. At $M_{K_S} < 8$, the mean of $\Delta \log R'_{\rm HK}$ is only 0.10 dex, however for $M_{K_S} > 8$, the mean is 0.56 dex. The star with the highest difference in $\log R'_{\rm HK}$ is GJ 1002, which has $\Delta \log R'_{\rm HK} = 1.31$ dex. This is because of its wide range of $T_{\rm eff}$ calibrations, with $\Delta T_{\rm eff} = 534$ K.

4.2. Chromospheric H-alpha flux

In Fig. 9, we correct for the photospheric contribution and plot the chromospheric flux ratio of Hα, $\mathcal{F}'_{\rm H\alpha}/\mathcal{F}_{\rm bol}$. This is not on a logarithmic scale, unlike how we plot $\log R'_{\rm HK}$. This is because the sign of $\mathcal{F}'_{\rm H\alpha}/\mathcal{F}_{\rm bol}$ indicates whether the line is in emission or absorption. Values of $\mathcal{F}'_{\rm H\alpha}/\mathcal{F}_{\rm bol} \sim 0$ indicate that Hα is filled to the continuum. Values $\mathcal{F}'_{\rm H\alpha}/\mathcal{F}_{\rm bol} > 0$ indicate that Hα is in emission, as in Fig. 5, while values $\mathcal{F}'_{\rm H\alpha}/\mathcal{F}_{\rm bol} < 0$ indicate that Hα is in absorption as in Fig. 4. The plotting colors and symbols are the same as used in Fig. 8.

For stars with Hα in absorption, $\mathcal{F}'_{\rm H\alpha}/\mathcal{F}_{\rm bol}$ increases toward a filling-in of the continuum toward larger M_{K_S}. The stars in which Hα is in emission tend to have significantly higher $\mathcal{F}'_{\rm H\alpha}/\mathcal{F}_{\rm bol}$ than stars for which Hα is near the continuum level. We note that the absorption of Hα stays in a relatively narrow range. Values of $\mathcal{F}'_{\rm H\alpha}/\mathcal{F}_{\rm bol}$ are $-0.6 \cdot 10^{-4} < \mathcal{F}'_{\rm H\alpha}/\mathcal{F}_{\rm bol} \lesssim 0$. However, for stars in which Hα is in emission, the range of $\mathcal{F}'_{\rm H\alpha}/\mathcal{F}_{\rm bol}$ is on the order of several 10^{-4}. larger $\Delta\mathcal{F}'_{\rm H\alpha}/\mathcal{F}_{\rm bol}$ due to the different $T_{\rm eff}$ calibrations. Stars for which Hα is in emission also have significantly higher values of $R'_{\rm HK}$ than those in which Hα is not in emission.

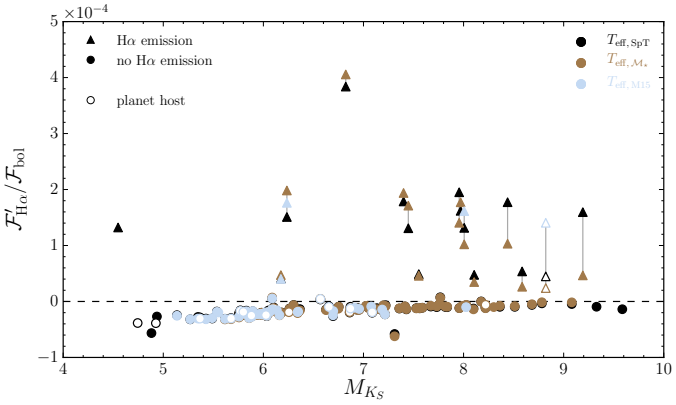

Fig. 9. Fractional chromospheric Hα flux, $\mathcal{F}'_{\rm H\alpha}/\mathcal{F}_{\rm bol}$, as a function of absolute magnitude M_{K_S}. Vertical gray lines connect different measurements of the same star. Triangles indicate stars exhibiting Hα emission. Filled symbols indicate stars without known planetary systems, and open symbols indicate stars with known planetary systems. Values > 0 indicate that Hα is in emission, and values < 0 indicate that Hα is in absorption. Values near 0 indicate filling-in of the line to the continuum.

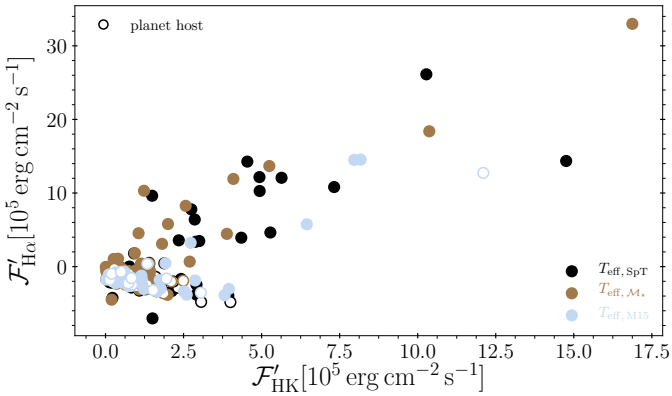

Fig. 10. Fractional chromospheric Hα flux, $\mathcal{F}'_{\rm H\alpha}$, as a function of fractional chromospheric Ca II H and K flux, $\mathcal{F}'_{\rm HK}$ flux. Filled symbols indicate stars without known planetary systems, and open symbols indicate stars with known planetary systems. Values > 0 indicate that Hα is in emission, and values < 0 indicate that Hα is in absorption. Values near 0 indicate filling-in of the line to the continuum.

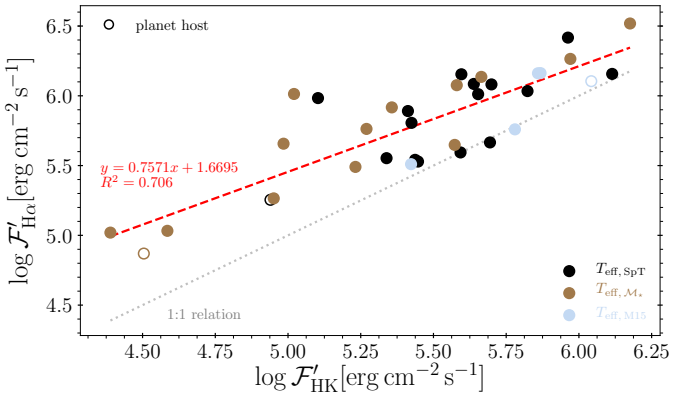

Fig. 11. Fractional chromospheric Hα flux, $\mathcal{F}'_{\rm H\alpha}$, as a function of fractional chromospheric Ca II H and K flux, $\mathcal{F}'_{\rm HK}$ flux, both on a logarithmic scale. Filled symbols indicate stars without known planetary systems, and open symbols indicate stars with known planetary systems. In this plot, only stars with Hα in emission (> 0) are shown. A linear fit is shown with a dashed red line, and a 1:1 relation is plotted as a dotted gray line.

4.3. H-alpha versus calcium II H and K flux

We plot chromospheric flux values of Hα against Ca II H and K in Figs. 10 and 11. Figure 10 contains flux in absolute flux units, and therefore contains negative values of Hα that correspond to absorption. Figure 11 shows flux on a log-scale and excludes inactive stars with Hα in absorption. Symbols and markers are the same as in Figures 8 and 9.

Fig. 10 shows Hα only in absoprtion ($\mathcal{F}'_{\rm H\alpha} \lesssim 0$), and a decreasing trend is apparent where it goes deeper into absorption with increasing $\mathcal{F}'_{\rm HK}$. The trend appears to be linear from $0.0 \leq \mathcal{F}'_{\rm HK} \leq 4.0 \cdot 10^{-5}$ erg cm^{-2} s^{-1}. When Hα is in emission, the trend of $\mathcal{F}'_{\rm H\alpha}$ increases with increasing $\mathcal{F}'_{\rm HK}$. This deepening of the Hα line before filling-in and going into emission was reported by Walkowicz & Hawley (2009) and Scandariato et al. (2017). Scandariato et al. (2017) only observed a decreasing trend from $0.0 \leq \mathcal{F}'_{\rm HK} \leq 1.0$. In Fig. 11, we overplot as a dashed red line a linear fit that we find to be

$$\log \mathcal{F}'_{\rm H\alpha} = 0.7571 \log \mathcal{F}'_{\rm HK} + 1.6695, \tag{14}$$

with $R^2 = 0.706$.

4.4. Ca II H and K surface flux calibrations

We compared calibrations of the continuum conversion factor $C_{\rm cf}$ (used for measuring $F_{\rm HK}$) of other studies with $C_{\rm cf}$ calibrations using the PHOENIX model grid. To derive our $T_{\rm eff}$ dependent conversion factor $C_{\rm cf}$, we combined Eq. 2, Eq. 3, and $S = 8\alpha\,(\mathcal{F}_{\rm HK}/\mathcal{F}_{RV})$, to arrive at

$$C_{\rm cf} = \frac{10^{14}}{8\alpha K}\frac{\mathcal{F}_{\rm RV}}{T_{\rm eff}^4}. \tag{15}$$

Using values of $\alpha = 2.4$ and $K = 1.07 \cdot 10^6$ erg cm^{-2} s^{-1} (Hall et al. 2007), we then obtained

$$C_{\rm cf} = 4.8676 \cdot 10^6 \cdot \frac{\mathcal{F}_{\rm RV}}{T_{\rm eff}^4}. \tag{16}$$

The top panel of Fig. 12 shows our computed $\log C_{\rm cf}$ as a function of $T_{\rm eff}$. Different values of [Fe/H] are shown as a function of color, and different values of $\log(g)$ are plotted with different symbols. For $T_{\rm eff} > 5000$ K, we used $\log(g)$ values of 4.0 and 4.5, and for $T_{\rm eff} \leq 5000$ K, we used $\log(g)$ values of 4.5 and 5.0. A fifth-order polynomial,

$$\log C_{\rm cf} = a + bT_{\rm eff} + cT_{\rm eff}^2 + dT_{\rm eff}^3 + eT_{\rm eff}^4 + fT_{\rm eff}^5, \tag{17}$$

was fit to all of the points and overplotted as a solid red line. The coefficients of this polynomial are listed in Table 2. We provide the computed PHOENIX stellar atmosphere $\log C_{\rm cf}$ values in Table D.4 for the entire model grid.

Table 2. $\log C_{\rm cf}$ vs. $T_{\rm eff}$ fifth-order polynomial fit coefficients

Parameter	Value
a	-2.9679E+01
b	2.6864E-02
c	-1.0268E-05
d	1.9866E-09
e	-1.9017E-13
f	7.1548E-18

Notes. Coefficients for calculating $\log C_{\rm cf}$ as a function of $T_{\rm eff}$ using the equation $\log C_{\rm cf} = a + bT_{\rm eff} + cT_{\rm eff}{}^2 + dT_{\rm eff}{}^3 + eT_{\rm eff}{}^4 + fT_{\rm eff}{}^5$.

Even for the wide range of metallicity values, the spread of $\log C_{\rm cf}$ is not too wide for $T_{\rm eff} > 3400$ K. For these higher temperatures, $\log C_{\rm cf}$ varies by 0.25 dex at most. At $T_{\rm eff} < 3100$ K, metallicity begins to contribute to a larger spread of $\log C_{\rm cf}$ values, around 0.5 dex. This spread of $\log C_{\rm cf}$ increases to 1.4 dex as $T_{\rm eff}$ decreases to 2300 K.

The bottom panel of Fig. 12 compares the polynomial fit in the upper panel with previously published $\log C_{\rm cf}$-$T_{\rm eff}$ relations (see Sec. A for details about the relations). For the relations of the other authors, we plot the range for which the relations are calibrated. Our $\log C_{\rm cf}$ values agree well with those from other studies for $T_{\rm eff} \gtrsim 4100$ K to ~ 0.1 dex. At temperatures cooler than 4100 K, our $\log C_{\rm cf}$ values start to deviate from those of Middelkoop (1982), Rutten (1984), Cincunegui et al. (2007), Suárez Mascareño et al. (2015), and Astudillo-Defru et al. (2017); our values are higher for cooler temperatures. For temperatures cooler than $T_{\rm eff} = 4100$ K, $\log C_{\rm cf}$ diverges by more than 0.2 dex. The difference between our relation and Cincunegui et al. (2007) increases to 0.4 dex at $T_{\rm eff} = 3100$ K, while the difference between our relation and both Suárez Mas-

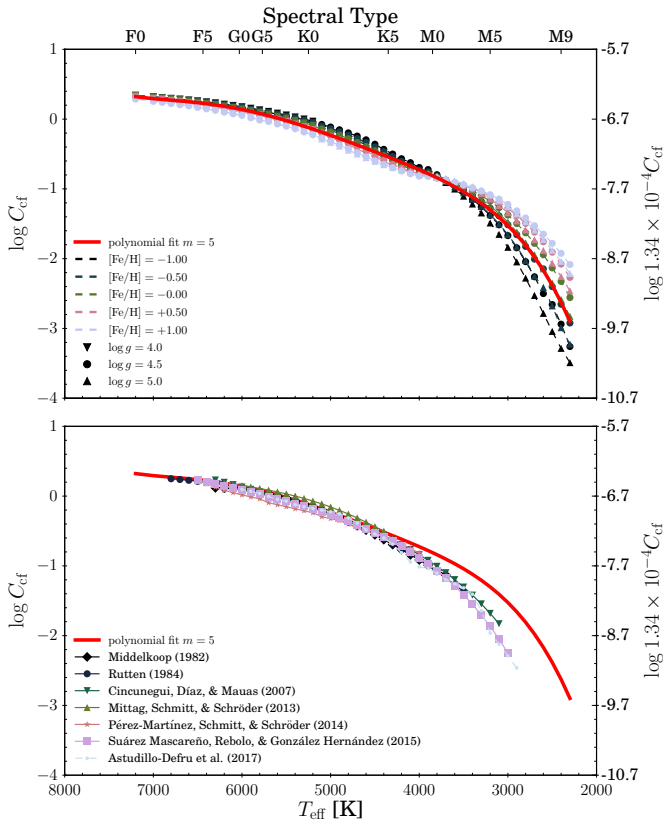

Fig. 12. Different $\log C_{cf}$ calibrations as a function of T_{eff}. The approximate spectral type is shown on the top axis. *Top*: PHOENIX stellar atmosphere models with different [Fe/H] and $\log(g)$, where [Fe/H] is indicated by color and $\log(g)$ indicated by symbol. The solid red line indicates a fifth-order polynomial fit. *Bottom*: Calibrations of $\log C_{cf}$ from other works where only the valid calibration region is plotted. Overplotted in red is the same fifth-order polynomial fit from the top panel.

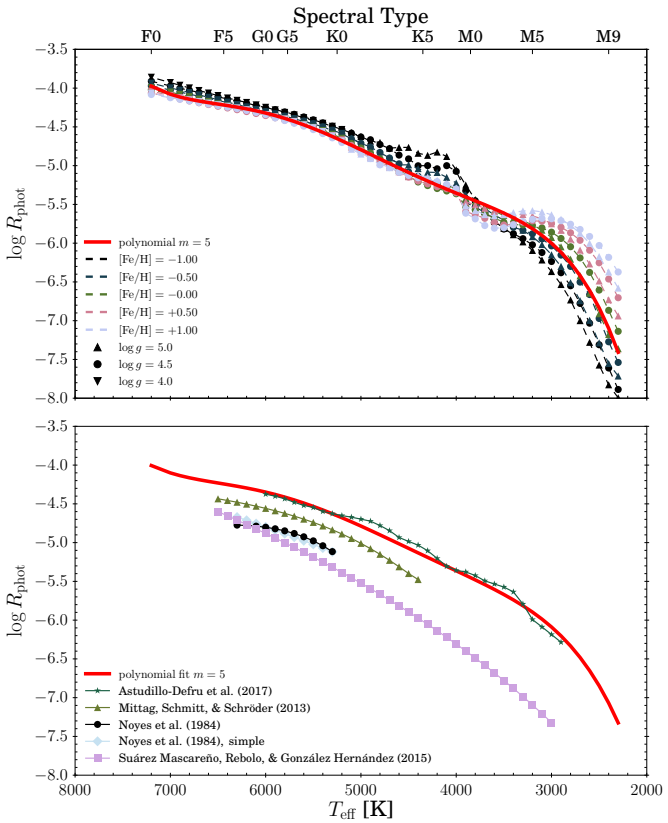

Fig. 13. Different $\log R_{HK,phot}$ as a function of T_{eff}. The approximate spectral type is shown on the top axis. *Top*: PHOENIX stellar atmosphere models with different [Fe/H] and $\log(g)$, where [Fe/H] is indicated by color and $\log(g)$ indicated by symbol. The solid red line indicates a fifth-order polynomial fit. *Bottom*: Calibrations of $\log R_{HK,phot}$ from other works where only the valid calibration region is plotted. Overplotted in red is the same fifth-order polynomial fit from the top panel.

careño et al. (2015) and Astudillo-Defru et al. (2017) increases to 0.8 dex at $T_{eff} = 3000$ K. This discrepency in $\log C_{cf}$ might be attributed to the use of empirical calibrations with these studies as opposed to this work using stellar models (see Sec. 5).

As an example, when we take for the Sun $B - V = 0.642$ and $S_{MWO} = 0.164$, the Noyes et al. (1984) calibration of R_{HK} will give us $\log R_{HK} = -4.62$. Our calibration using Eq. 17 results in $\log R_{HK} = -4.60$. This means that for a Sun-like star, $\Delta \log R_{HK} = 0.02$.

4.5. Ca II H and K photospheric flux calibrations

In the top panel of Fig. 13, we plot $\log R_{HK,phot}$ as a function of T_{eff}, computed as described in Sec. 3.2. The colors and symbols are assigned in the same manner as in Fig. 12. A fifth-order polynomial fit

$$\log R_{HK,phot} = a + bT_{eff} + cT_{eff}^2 + dT_{eff}^3 + eT_{eff}^4 + fT_{eff}^5, \quad (18)$$

is overplotted as a solid red line, and coefficients of this polynomial are listed in Table 3. Similarly as with $\log C_{cf}$, metallicity has an effect on the spread of $\log R_{HK,phot}$ values. The spread increases at $4000 \leq T_{eff} \leq 5100$ K and $T_{eff} \leq 3800$ K. At $T_{eff} > 5100$ K, the spread of $\log R_{HK,phot}$ values is lower than 0.2 dex. The spread increases from $T_{eff} = 5100$ K to $T_{eff} = 4200$ K, where it is about 0.4 dex. At $T_{eff} = 3100$ K, the spread of $\log R_{HK,phot}$ is 0.6 dex. Here, a change in metallicity of ±0.5 dex can result in a $\Delta \log R_{HK,phot} \sim 0.1$ dex. At $T_{eff} < 3300$ K, the spread continually increases with lower temperatures to almost 1.6 dex at $T_{eff} = 2400$ K. At $T_{eff} = 2400$ K., a change in metallicity of ±0.5 can result in a $\Delta \log R_{HK,phot} \sim 0.5$ dex. We provide the computed PHOENIX stellar atmosphere $\log R_{HK,phot}$ values in Table D.4 for the entire model grid.

In the bottom panel of Fig. 13, we compare our $\log R_{HK,phot}$-T_{eff} polynomial fit with previous literature relations (see Sec. B for details about the relations). The higher $\log R_{HK,phot}$ values of both Mittag et al. (2013) and our work in comparison with Noyes et al. (1984) and Suárez Mascareño et al. (2015) are clear. The difference between Mittag et al. (2013) and Noyes et al. (1984) is $\sim$ 0.3 dex, and the difference between our work and Noyes et al. (1984) ranges from 0.4 to 0.5 dex. The difference between our work and Suárez Mascareño et al. (2015) can be as large as 1.3 dex at $T_{eff} = 3000$ K. Our values of $\log R_{HK,phot}$ agree very well with those of Astudillo-Defru et al. (2017), with the largest difference being 0.12 dex at $T_{eff} = 4800$ K, and other differences on the order of 0.1 dex at $T_{eff} = 3500$ K, 3400 K, and 3100 K.

Our $\log R_{HK,phot}$ calibration has much higher values than the calibration used by Noyes et al. (1984). This systematic offset was also observed by Astudillo-Defru et al. (2017), who also used synthetic spectra to obtain an $R_{HK,phot}$ calibration. While the exact reason for this offset is not known (see the discussion in Astudillo-Defru et al. (2017)), an offset correction can be ap-

Table 3. $\log R_{\rm HK,phot}$ vs. $T_{\rm eff}$ fifth-order polynomial fit coefficients

Parameter	Value
a	-3.7550E+01
b	3.2131E-02
c	-1.3177E-05
d	2.7133E-09
e	-2.7466E-13
f	1.0887E-17

Notes. Coefficients for calculating $\log R_{\rm HK,phot}$ as a function of $T_{\rm eff}$ using the equation $\log R_{\rm HK,phot} = a + bT_{\rm eff} + cT_{\rm eff}^2 + dT_{\rm eff}^3 + eT_{\rm eff}^4 + fT_{\rm eff}^5$.

plied to scale our $\log R_{\rm HK,phot}$ calibration to Noyes et al. (1984),

$$\log R_{\rm phot,N84} = \log R_{\rm phot,ours} - 0.4612, \quad (19)$$

where 0.4612 is the offset correction. This simple offset correction scales our $\log R_{\rm HK,phot}$ values to Noyes et al. (1984) values in their valid calibration region, so that our calibration can be used to obtain comparable results to Noyes et al. (1984), and also to extend the calibration to later-type stars. We note that although they are widely used, the Noyes et al. (1984) calibrations are only calibrated in the range 5300 K $\lesssim T_{\rm eff} \lesssim$ 6300 K.

If we take the same $B-V$ and $S_{\rm MWO}$ values as in Sec. 4.4, the Noyes et al. (1984) calibration of $R_{\rm HK,phot}$ will give us $\log R_{\rm HK,phot} = -4.92$. This will give us an activity measurement of $\log R'_{\rm HK} = -4.92$. Our calibration using Eq. 19 results in $\log R_{\rm HK,phot} = -4.89$, which gives us $\log R'_{\rm HK} = -4.91$. Then, for a Sun-like star, $\Delta \log R_{\rm HK,phot} = 0.03$ and $\Delta \log R'_{\rm HK} = 0.01$.

4.6. χ-factor

The χ-factor provides a method to convert the equivalent width of Ca II H and K into $R_{\rm HK}$ and Hα indto $\mathcal{F}_{\rm H\alpha}/\mathcal{F}_{\rm bol}$ in M dwarfs. Walkowicz et al. (2004) define the χ factor as the ratio of the $H\alpha$ line continuum luminosity to bolometric luminosity, namely

$$\chi = L_{\rm H\alpha,cont}/L_{\rm bol}, \quad (20)$$

where $L_{\rm H\alpha,cont}$ is the luminosity of a selected continuum region near Hα. West & Hawley (2008) extend the selection of χ values to higher-order Balmer lines and Ca II H and K. When multiplied by the equivalent width of the respective line, we can obtain the ratio of the line luminosity to the bolometric luminosity,

$$L_{\rm line}/L_{\rm bol} = \chi_{\rm line} \cdot {\rm EW}_{\rm line}. \quad (21)$$

For both Ca II H and K and Hα, we calculated the χ values of West & Hawley (2008) of the PHOENIX model grid for M dwarf $T_{\rm eff}$ values and different metallicities, constraining $\log(g) = 5.0$. For Ca II H and K, we used the continuum regions given by Walkowicz & Hawley (2009), and for Hα, we used the continuum regions given by West & Hawley (2008). We plot these with the values listed in West & Hawley (2008) in Fig. 14, with Ca II H and K in the top panel and Hα in the lower panel. We provide the computed $\chi_{\rm line}$ values in Table D.5.

Similar to Fig. 12, the continuum values diverge as $T_{\rm eff}$ decreases for different metallicities. For $\chi_{\rm CaIIHK}$, a metallicity of [Fe/H] = −0.5 agrees best with West & Hawley (2008). We note that all of our $\chi_{\rm CaIIHK}$ values are higher for M3 and M4 spectral types. However, this difference is very small (on the order of 10^{-7}), and the error bars of West & Hawley (2008) are much smaller than the spread of $\chi_{\rm CaIIHK}$ by metallicity. Our $\chi_{\rm H\alpha}$ values also agree well with West & Hawley (2008), especially for [Fe/H] = 0.0. Our $\chi_{\rm H\alpha}$ values deviate from West & Hawley (2008) at spectral types M4 and earlier. However, like with $\chi_{\rm CaIIHK}$, the difference is small, on the order of 10^{-6}.

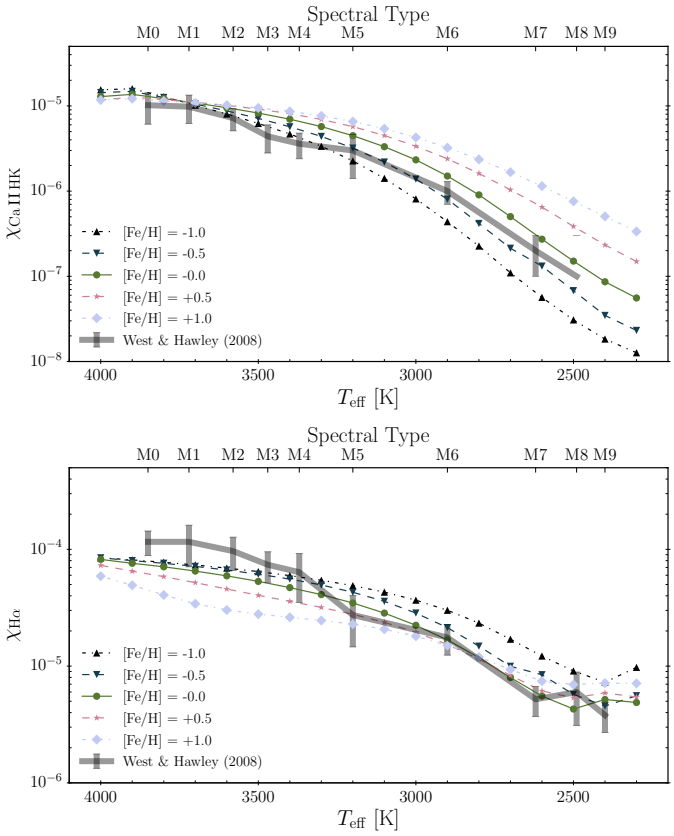

Fig. 14. *Top*: Continuum flux normalized to bolometric flux of Ca II H and K, $\chi_{\rm CaIIHK}$, as a function of $T_{\rm eff}$ using PHOENIX stellar atmospheres with $\log(g) = 5.0$ and different metallicities. Values from West & Hawley (2008) are plotted in gray. *Bottom*: Continuum flux normalized to bolometric flux of Hα, $\chi_{\rm H\alpha}$, as a function of $T_{\rm eff}$ using PHOENIX stellar atmospheres with $\log(g) = 5.0$ and different metallicities. Values from West & Hawley (2008) are plotted in gray.

4.7. Proxima Centauri

Proxima Centauri, or GJ 551, is the only star in this study that exhibits Hα emission and is a known planet host (Anglada-Escudé et al. 2016). This indicator of high activity is consistent with the findings of Ribas et al. (2016), who reported that Proxima b receives ten times more far-UV flux than the current Earth.

Except for the $T_{\rm eff,M15}$ calibration of Proxima Centauri ($\log R'_{\rm HK} = -3.92$, $T_{\rm eff,M15} = 3555$ K), we did not measure $\log R'_{\rm HK} > -4.5$ for any planet hosts. However, this particular value may be overestimated. For example, for Proxima Centauri, Boyajian et al. (2012) reported $T_{\rm eff} \sim 3050$ K, and the calibration of $T_{\rm eff,SpT} = 2900$ K, which has $\log R'_{\rm HK} = -4.59$. The similarities between these two temperatures mean that $\log R'_{\rm HK}$ of Proxima Centauri probably sits closer to ~ -4.5 than ~ -3.9.

5. Discussion

With the exception of Proxima Centauri, which exhibits Hα in emission, the remaining known planet hosts exhibit low activity. This is expected as activity can mimic planetary signals and

cause incorrect planet detections, so that stars with lower activity stars are preferred for planet searches.

There is a divergence of $\log C_{\rm cf}$ values between our work and other works that begins at the start of the M dwarf sequence near 4000 K. Middelkoop (1982), Rutten (1984), Cincunegui et al. (2007), Suárez Mascareño et al. (2015), and Astudillo-Defru et al. (2017) used observational data to calibrate $\log C_{\rm cf}$ as a function of $B-V$, while we used stellar models as a function of $T_{\rm eff}$. The discrepency might be due to an insufficient $(B-V)-T_{\rm eff}$ relation in this region. However, our $\chi_{\rm CaIIHK}$ values agree with those of West & Hawley (2008), whose relations were also derived from observational data. This gives us confidence that the PHOENIX models are accurate in the continuum near the Ca II H and K lines, although the continuum region of $\chi_{\rm CaIIHK}$ differs from the region used in $\log C_{\rm cf}$.

Our $\log R_{\rm HK,\,phot}$ values remain higher than $\log R_{\rm HK,\,phot}$ values obtained using observational data (Noyes et al. 1984; Suárez Mascareño et al. 2016). As noted by Mittag et al. (2013), this difference arises from the integration region of the calcium line. Our work and Mittag et al. (2013) both integrated the entire photospheric line. The $\log R_{\rm HK,\,phot}$ relation used by Noyes et al. (1984) is that of Hartmann et al. (1984), who only estimated the flux outside of the line core exterior to the H1 and K1 points: they assumed the flux of the line core to be zero. The $\log R_{\rm HK,\,phot}$ relation derived by Suárez Mascareño et al. (2015) also masks the line core: 0.7 Å for FGK stars, and 0.4 Å for M stars. For this reason, we provide the correction factor in Eq. 19 to keep the calculated $R'_{\rm HK}$ values consistent with historical published measurements based on Noyes et al. (1984). Moreover, although both use PHOENIX models, our $\log R_{\rm HK,\,phot}$ values are still higher than those of Mittag et al. (2013). One reason for this difference might be the models that were used; Mittag et al. (2013) used models computed in non-local thermodynamic equilibrium, while we used models computed in local thermodynamic equilibrium.

Astudillo-Defru et al. (2017) measured $R'_{\rm HK}$ of 403 stars of the HARPS M dwarf sample. They extended the technique of Noyes et al. (1984) by calibrating their own $\log C_{\rm cf}$ using 14 G or K and M dwarf pairs and use BT-Settl models to arrive at $R_{\rm HK,\,phot}$ through an S-index conversion. Although we used different methods to arrive at the measurement of $R'_{\rm HK}$ in M dwarfs, we find our results to be consistent with Astudillo-Defru et al. (2017). Namely, our Fig. 8 exhibits a very similar lower envelope of $R'_{\rm HK}$ values to their Fig. 10. For brighter M_{K_S} values (earlier-M dwarf types), we find a relatively constant lower envelope of $R'_{\rm HK}$ values (see Fig. 8), while Astudillo-Defru et al. (2017) also reported a constant lower envelope of $R'_{\rm HK}$ for the higher M dwarf masses (see their lower Fig. 10). As M_{K_S} increases and M dwarf types move to later types, the lower envelope of $R'_{\rm HK}$ values begins to decrease. Finally, this lower envelope flattens out again for lower masses, or later spectral types. Mittag et al. (2013) similarly reported that the initially constant lower envelope was followed by a decreasing lower envelope. We note a key difference in our findings in that the technique used to derive $T_{\rm eff}$ influences the extent of the decreasing lower envelope and then the level of the constant envelope for the lowest masses. However, each method individually still exhibits this behavior.

Surveys that focus on determining stellar parameters (e.g., Maldonado et al. (2015)) would be the more reliable source of stellar parameters if the given star were included in that survey. Moreover, when the S-index of a given star is the sole measurement and no access to any spectra is possible, then we recommend the use of Eq. 17 and Eq. 18 to calculate $R'_{\rm HK}$.

6. Summary and conclusions

In this work, we have measured Ca II H and K and Hα activity in a large sample of HARPS M dwarf spectra using high S/N template spectra and PHOENIX model atmospheres. We compared three different $T_{\rm eff}$ calibrations and find $\Delta T_{\rm eff} \sim$ several 100 K for mid- to late-M dwarfs. This uncertainty in $T_{\rm eff}$ contributes up to $\Delta \log R'_{\rm HK} = 1.31$ dex and $\Delta \log \mathcal{F}'_{\rm H\alpha}/\mathcal{F}_{\rm bol} = 2.93$ dex. We have extended $R'_{\rm HK}$ calibrations to the M dwarf regime using PHOENIX model spectra. We compared these new $R'_{\rm HK}$ calibrations with previous calibrations. Our $\log C_{\rm cf}$ calibration agrees very well with previous calibrations within 0.2 dex, and extends the calibration from 3100 K $\leq T_{\rm eff} \leq$ 6800 K to 2300 K $\leq T_{\rm eff} \leq$ 7200 K. Our $\log R_{\rm HK,\,phot}$ calibration overstimates the Noyes et al. (1984) calibration by 0.46 dex. However, our calibration extends $\log R_{\rm HK,\,phot}$ to 2300 K $\leq T_{\rm eff} \leq$ 7200 K, and a simple offset correction can be applied to scale our $\log R_{\rm HK,\,phot}$ to that of Noyes et al. (1984). We have provided a grid of $\log C_{\rm cf}$ and $\log R_{\rm HK,\,phot}$ values as functions of $T_{\rm eff}$, [Fe/H], and $\log(g)$. This grid can be used to compute $R'_{\rm HK}$ from S-index values using either polynomial fits to or an interpolation of the grid, and can be further beneficial when constraints on the stellar parameters of the targets are established. We have calculated $\chi_{\rm CaIIHK}$ and $\chi_{\rm H\alpha}$ for $-1.0 \leq$ [Fe/H] $\leq +1.0$ in steps of Δ[Fe/H] = 0.5 for the entire M dwarf $T_{\rm eff}$ range. We find that our χ values from PHOENIX models agree well with the χ values of West & Hawley (2008).

We find that the lower boundary of $\log R'_{\rm HK}$ either stays constant or decreases with later-M dwarfs depending on the $T_{\rm eff}$ calibration used. Because of conflicting $T_{\rm eff}$ measurements toward later-M dwarfs, an accurate determination of $R'_{\rm HK}$ cannot be made beyond $M_{K_S} > 8$. For $\mathcal{F}'_{\rm H\alpha}/\mathcal{F}_{\rm bol}$, the lower boundary of inactive stars begins with early-M dwarfs in deeper absorption, and fills in to the continuum towards later-M dwarfs. Stars with known planetary systems do not exhibit unexpected or peculiar levels of Ca II H, K, and Hα activity in relation to stars of similar spectral type or absolute magnitude.

Our surface flux calibration of $\log C_{\rm cf}$ agrees very well with that of Middelkoop (1982) for FGK stars, and our surface flux calibrations of $\chi_{\rm CaIIHK}$ and $\chi_{\rm H\alpha}$ also agree well with those of West & Hawley (2008) for M stars. Our $R'_{\rm HK}$ calibrations agree very well with those of Noyes et al. (1984) to within $\Delta \log R'_{\rm HK} = 0.01$ dex for the Sun. We conclude that our calibrations are a reliable extension to previous $R'_{\rm HK}$ calibrations, provide a consistent way to measure $R'_{\rm HK}$ across spectral types early F to late M, and allow the comparison of activity of Sun-like stars to M dwarfs.

Acknowledgements. We thank Tim-Oliver Husser for fruitful discussions and providing us with recalculated PHOENIX models. The authors acknowledge research funding by the Deutsche Forschungsgemeinschaft (DFG) under the grant SFB 963, project A04. SVJ acknowledges the support of the DFG priority program SPP 1992 "Exploring the Diversity of Extrasolar Planets" (JE 701/5-1). SBS acknowledges the support of the Austrian Science Fund (FWF) Lise Meitner project M2829-N. This work is based on data products from observations made with ESO Telescopes at the La Silla Observatory (Chile) under the program IDs 60.A-9036, 072.C-0488, 074.C-0364, 075.C-0202, 075.D-0614, 076.C-0155, 077.C-0364, 078.C-0044, 082.C-0718, 085.C-0019, 086.C-0284, 087.C-0831, 089.C-0050, 089.C-0732, 090.C-0395, 090.C-0421, 091.C-0034, 180.C-0886, 183.C-0437, 183.C-0972, 185.D-0056, 191.C-0505, 192.C-0224, and 283.C-5022. We acknowledge the effort of all the observers of the aforementioned ESO projects whose data we have used.

References

Anglada-Escudé, G., Amado, P. J., Barnes, J., et al. 2016, Nature, 536, 437
Anglada-Escudé, G., Arriagada, P., Tuomi, M., et al. 2014, MNRAS, 443, L89
Anglada-Escudé, G. & Butler, R. P. 2012, ApJS, 200, 15

Astudillo-Defru, N., Delfosse, X., Bonfils, X., et al. 2017, A&A, 600, A13
Baliunas, S. L., Donahue, R. A., Soon, W. H., et al. 1995, ApJ, 438, 269
Barden, S. C. 1985, ApJ, 295, 162
Berdinas, Z. M., Amado, P. J., & Anglada-Escude, G. 2015, in Cambridge Workshop on Cool Stars, Stellar Systems, and the Sun, Vol. 18, 18th Cambridge Workshop on Cool Stars, Stellar Systems, and the Sun, ed. G. T. van Belle & H. C. Harris, 723–732
Bonfils, X., Delfosse, X., Udry, S., et al. 2013, A&A, 549, A109
Boro Saikia, S., Marvin, C. J., Jeffers, S. V., et al. 2018, A&A, 616, A108
Boyajian, T. S., von Braun, K., van Belle, G., et al. 2012, ApJ, 757, 112
Cincunegui, C., Díaz, R. F., & Mauas, P. J. D. 2007, A&A, 469, 309
Delfosse, X., Forveille, T., Ségransan, D., et al. 2000, A&A, 364, 217
Duncan, D. K., Vaughan, A. H., Wilson, O. C., et al. 1991, ApJS, 76, 383
Golimowski, D. A., Henry, T. J., Krist, J. E., et al. 2004, AJ, 128, 1733
Gomes da Silva, J., Santos, N. C., Bonfils, X., et al. 2011, A&A, 534, A30
Gray, D. F. 2005, The Observation and Analysis of Stellar Photospheres
Hall, J. C., Lockwood, G. W., & Skiff, B. A. 2007, AJ, 133, 862
Hartmann, L., Soderblom, D. R., Noyes, R. W., Burnham, N., & Vaughan, A. H. 1984, ApJ, 276, 254
Herbig, G. H. 1985, ApJ, 289, 269
Husser, T.-O., Wende-von Berg, S., Dreizler, S., et al. 2013, A&A, 553, A6
Kenyon, S. J. & Hartmann, L. 1995, ApJS, 101, 117
Maldonado, J., Affer, L., Micela, G., et al. 2015, A&A, 577, A132
Maldonado, J., Scandariato, G., Stelzer, B., et al. 2017, A&A, 598, A27
Mann, A. W., Feiden, G. A., Gaidos, E., Boyajian, T., & von Braun, K. 2015, ApJ, 804, 64
Martínez-Arnáiz, R., López-Santiago, J., Crespo-Chacón, I., & Montes, D. 2011, MNRAS, 414, 2629
Middelkoop, F. 1982, A&A, 107, 31
Mittag, M., Schmitt, J. H. M. M., & Schröder, K.-P. 2013, A&A, 549, A117
Montes, D., de Castro, E., Fernandez-Figueroa, M. J., & Cornide, M. 1995a, A&AS, 114, 287
Montes, D., Fernandez-Figueroa, M. J., de Castro, E., & Cornide, M. 1995b, A&A, 294, 165
Neves, V., Bonfils, X., Santos, N. C., et al. 2012, A&A, 538, A25
Neves, V., Bonfils, X., Santos, N. C., et al. 2014, A&A, 568, A121
Newton, E. R., Irwin, J., Charbonneau, D., et al. 2017, ApJ, 834, 85
Noyes, R. W., Hartmann, L. W., Baliunas, S. L., Duncan, D. K., & Vaughan, A. H. 1984, ApJ, 279, 763
Passegger, V. M., Wende-von Berg, S., & Reiners, A. 2016, A&A, 587, A19
Pepe, F., Mayor, M., Rupprecht, G., et al. 2002, The Messenger, 110, 9
Perdelwitz, V., Mittag, M., Tal-Or, L., et al. 2021, A&A, 652, A116
Pérez Martínez, M. I., Schröder, K.-P., & Hauschildt, P. 2014, MNRAS, 445, 270
Rauscher, E. & Marcy, G. W. 2006, PASP, 118, 617
Reiners, A. & Basri, G. 2007, ApJ, 656, 1121
Reiners, A. & Mohanty, S. 2012, ApJ, 746, 43
Reiners, A., Shulyak, D., Käpylä, P. J., et al. 2022, arXiv e-prints, arXiv:2204.00342
Ribas, I., Bolmont, E., Selsis, F., et al. 2016, A&A, 596, A111
Rutten, R. G. M. 1984, A&A, 130, 353
Scandariato, G., Maldonado, J., Affer, L., et al. 2017, A&A, 598, A28
Shulyak, D., Seifahrt, A., Reiners, A., Kochukhov, O., & Piskunov, N. 2011, MNRAS, 418, 2548
Suárez Mascareño, A., Rebolo, R., & González Hernández, J. I. 2016, A&A, 595, A12
Suárez Mascareño, A., Rebolo, R., González Hernández, J. I., & Esposito, M. 2015, MNRAS, 452, 2745
Vaughan, A. H. & Preston, G. W. 1980, PASP, 92, 385
Walkowicz, L. M. & Hawley, S. L. 2009, AJ, 137, 3297
Walkowicz, L. M., Hawley, S. L., & West, A. A. 2004, PASP, 116, 1105
Wenger, M., Ochsenbein, F., Egret, D., et al. 2000, A&AS, 143, 9
West, A. A. & Hawley, S. L. 2008, PASP, 120, 1161

Appendix A: Ca II H and K surface flux calibrations

Measuring $\log C_{\rm cf}$ of 85 main-sequence stars from the Vaughan & Preston (1980) survey of the solar neighborhood, Middelkoop (1982) fit a polynomial to $\log C_{\rm cf}$ as a function of $B-V$,

$$\log C_{\rm cf,\,M82} = 1.13(B-V)^3 - 3.91(B-V)^2 + 2.84(B-V) - 0.47 \tag{A.1}$$

for $0.45 \leq (B-V) \leq 1.50$.

Rutten (1984) extended the relation further by measuring 30 additional main-sequence stars and also 27 subgiants and giants,

$$\log C_{\rm cf,\,R84} = 0.25(B-V)^3 - 1.33(B-V)^2 + 0.43(B-V) + 0.24, \tag{A.2}$$

which is valid for main-sequence stars with $0.3 \leq (B-V) \leq 1.6$.

Cincunegui et al. (2007) extended the calibration using 109 stars ranging from spectral type F6 to M5,

$$\log C_{\rm cf,\,CDM07} = -0.33(B-V)^3 - 0.55(B-V)^2 - 1.41(B-V) + 0.8 \tag{A.3}$$

for $0.45 \leq (B-V) \leq 1.81$. Middelkoop (1982), Rutten (1984), and Cincunegui et al. (2007) all made use of the relation of Noyes et al. (1984) to convert $B-V$ into $T_{\rm eff}$.

Instead of using observational spectra, Mittag et al. (2013) used PHOENIX stellar atmosphere models to measure $\mathcal{F}_{RV}$ directly in absolute flux units,

$$\log (\mathcal{F}_{RV}/19.2)_{\rm MSS13} = 8.33 - 1.79(B-V), \tag{A.4}$$

where $0.44 \leq (B-V) \leq 1.60$. They transformed this to $\log C_{\rm cf}$ using

$$\log C_{\rm cf} = 8.33 - 1.79(B-V) - \log\alpha - \log T_{\rm eff}^4 - 14, \tag{A.5}$$

where $\alpha = 19.2$, and used the $B-V$ to $T_{\rm eff}$ relation of Gray (2005).

Similarly, Pérez Martínez et al. (2014) also used PHOENIX models to derive a conversion factor

$$\log C_{\rm cf,\,PMSH14} = 0.66 - 1.11(B-V) \tag{A.6}$$

for $0.44 \leq (B-V) \leq 1.33$. Pérez Martínez et al. (2014) used the $B-V$ to $T_{\rm eff}$ tables of Schmidt-Kaler (1982) (which they also included in their publication).

Using HARPS spectra of FGKM stars, Suárez Mascareño et al. (2015) derived a continuum correction factor

$$\log C_{\rm cf,\,SM15} = 0.668 - 1.270(B-V) + 0.645(B-V)^2 - 0.443(B-V)^3 \tag{A.7}$$

for $0.4 \lesssim (B-V) \lesssim 1.9$.

Astudillo-Defru et al. (2017) empirically determine a continuum correction factor,

$$\log C_{\rm cf,\,AD17} = -0.203(B-V)^3 + 0.109(B-V)^2 - 0.972(B-V) + 0.669 \tag{A.8}$$

for $0.54 \leq (B-V) \leq 1.9$.

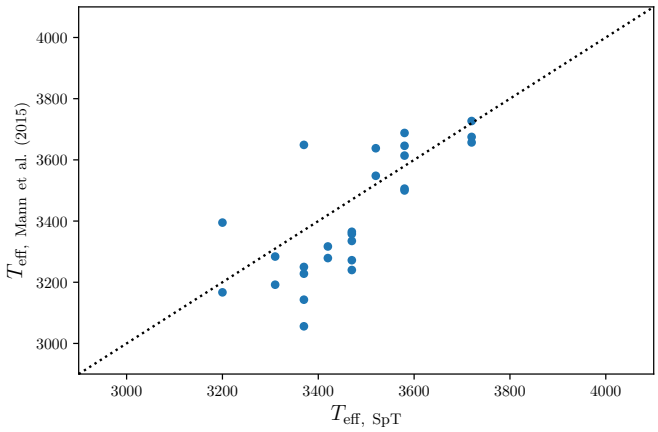

Fig. C.1. $T_{\rm eff}$ of Mann et al. (2015) vs $T_{\rm eff,\,SpT}$. The dotted line shows the 1:1 relation.

Appendix B: Ca II H and K photospheric flux calibrations

In their publication, Noyes et al. (1984) also provided an alternative, simpler form of Eq. 10 and obtained similar results within the valid calibration range,

$$\log R_{\rm phot,\,N84,simple} = -4.02 - 1.40(B-V). \tag{B.1}$$

Mittag et al. (2013), using PHOENIX stellar atmosphere models, reported two linear dependences of $\log R_{\rm HK,\,phot}$ on $B-V$ with for two $B-V$ ranges:

$$\log R_{\rm phot,\,MSS13} = 7.49 - 2.06(B-V) - \log\mathcal{F}_{\rm bol} \tag{B.2}$$

for $0.44 \leq B-V < 1.28$, and

$$\log R_{\rm phot,\,MSS13} = 6.19 - 1.04(B-V) - \log\mathcal{F}_{\rm bol} \tag{B.3}$$

for $1.28 \leq B-V < 1.60$.

Using HARPS spectra and a 0.7 Å rectangular mask of the line core for the most inactive FGK stars and a 0.4 Å rectangular mask for the most inactive M stars, Suárez Mascareño et al. (2015) fit a photospheric flux relation,

$$\log R_{\rm phot,\,SM15} = \log 1.48 \cdot 10^{-4} \exp -4.3658(B-V), \tag{B.4}$$

for $0.4 \lesssim (B-V) \lesssim 1.9$.

Astudillo-Defru et al. (2017) determined a photospheric flux relation using a synthetic spectrum, resulting in,

$$\log R_{\rm phot,\,AD17} = -0.045(B-V)^3 - 0.026(B-V)^2 - 1.036(B-V) - 3.749(B-V) \tag{B.5}$$

for $0.54 \leq (B-V) \leq 1.9$.

Appendix C: Effective temperature comparison with other calibrations

In Section 3.5 we presented three different $T_{\rm eff}$ calibrations that we used as stellar parameters in this study (see Fig. 7). Here in this appendix we present the $T_{\rm eff}$ measurements of common targets by Mann et al. (2015) to show agreement and the degree of agreement with the different $T_{\rm eff}$ calibration techniques.

Appendix D: Tables

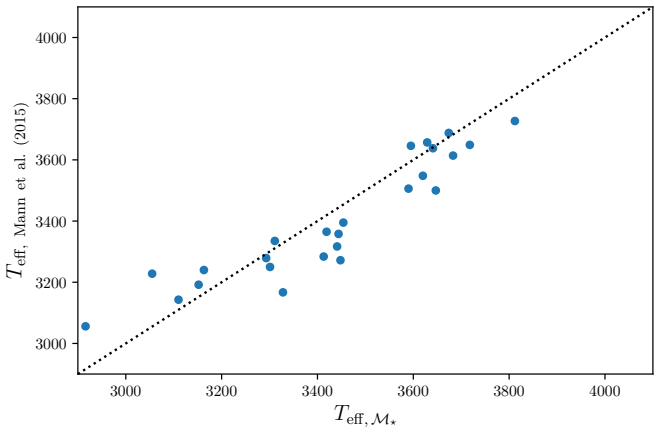

Fig. C.2. $T_{\rm eff}$ of Mann et al. (2015) vs $T_{\rm eff,\mathcal{M}_\star}$. The dotted line shows the 1:1 relation.

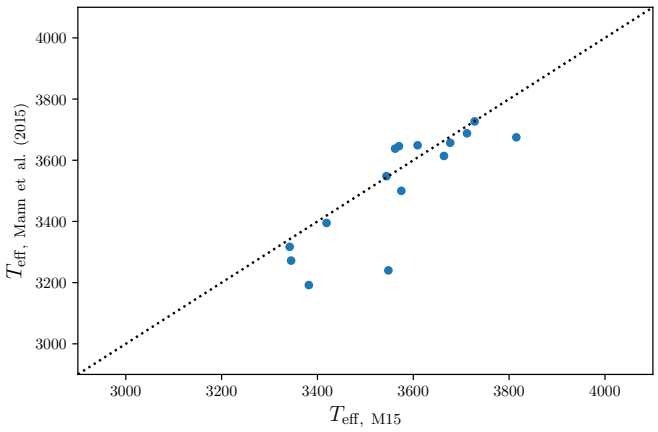

Fig. C.3. $T_{\rm eff}$ of Mann et al. (2015) vs $T_{\rm eff,M15}$. The dotted line shows the 1:1 relation.

Table D.1. Astronomical measurements of the sample of stars.

Name	α (2000)	δ (2000)	μ_α [mas yr^{-1}]	μ_δ [mas yr^{-1}]	π [mas]	Spec. type	B [mag]	V [mag]	K_S [mag]	M_{K_S} [mag]	$N_{\rm spectra}$
GJ 1	00:05:24.42828	-37:21:26.5010	5634.68	-2337.71	230.42	M1.5	10.0	8.6	4.5	6.3	47
GJ 1002	00:06:43.255	-07:32:14.71	-749.00	-1922.00	213.00	M5.5V	15.7	13.8	7.4	9.1	7
GJ 12	00:15:49.20	+13:33:21.9	621.00	333.00	84.00	M3	14.0	12.5	7.8	7.4	7
GJ 3049	00:43:26.031	-41:17:33.71	-775.00	-780.00	101.00	M3	14.0	···	7.7	7.7	6
GJ 54.1	01:12:30.63918	-16:59:56.3353	1208.53	640.73	271.01	M4Ve	13.9	12.1	6.4	8.6	21
L 707-74	01:23:18.029	-12:56:23.00	-12.30	335.20	97.80	M	13.8	12.8	8.3	8.3	5
GJ 87	02:12:20.98849	+03:34:32.2312	-1760.70	-1852.91	96.02	M2.5V	11.5	10.0	6.1	6.0	28
GJ 105B	02:36:15.357	+06:52:19.14	1813.00	1447.00	129.40	M4.5V	13.3	11.7	6.6	7.1	22
CD-44-836A	02:45:10.726	-43:44:31.64	40.00	-370.00	113.90	M4	13.9	12.3	7.3	7.6	8
CD-44-836B	02:45:14.31	-43:44:10.2	40.00	-350.00	142.86	M5	14.3	12.7	7.2	8.0	4
GJ 3189	02:58:10.21	-12:53:06.7	275.00	551.00	95.50	sdM3.0	14.4	12.7	8.2	8.1	10
GJ 3193B	03:01:51.38955	-16:35:36.1103	-356.78	-302.31	106.16	M3.0	12.2	10.5	6.5	6.6	9
GJ 3207	03:11:35.20	-38:47:23.4	838.00	-195.00	130.00	M3.5	13.0	11.5	9.0	9.6	6
GJ 1057	03:13:22.995	+04:46:29.37	1749.00	84.00	117.10	M5.0V	15.6	13.8	7.8	8.2	9
GJ 145	03:32:55.85736	-44:42:07.0185	-311.53	131.98	93.11	M2.5V	13.1	11.5	6.9	6.8	7
GJ 1061	03:35:59.69	-44:30:45.3	730.00	-330.00	271.92	M5.0V	15.0	13.1	6.6	8.8	7
GJ 1065	03:50:44.32	-06:05:40.0	-450.00	-1373.00	104.00	M3V	14.5	12.8	7.8	7.8	8
GJ 1068	04:10:28.156	-53:36:07.81	-2585.00	-2744.00	143.40	M4.5	15.5	13.6	7.9	8.7	18
GJ 166C	04:15:21.733	-07:39:17.36	-2239.00	-3419.00	198.24	M5Ve	12.8	11.2	6.0	7.4	4
GJ 176	04:42:55.77497	+18:57:29.4043	656.85	-1116.20	107.83	M2.5V	11.5	10.0	5.6	5.8	71
GJ 3323	05:01:57.469	-06:56:45.92	-550.00	-533.00	187.92	M4.0V	13.9	12.2	6.7	8.1	7
GJ 3325	05:03:20.08559	-17:22:24.7421	-226.51	-447.19	108.61	M3V	13.4	11.7	6.9	7.1	9
GJ 191	05:11:40.58112	-45:01:06.2899	6505.08	-5730.84	255.66	sdM1.0	10.4	8.9	5.0	7.1	97
GJ 203	05:28:00.15251	+09:38:38.1399	-190.30	-759.45	113.50	M3.5	14.1	12.4	7.5	7.8	11
GJ 205	05:31:27.39595	-03:40:38.0311	761.86	-2093.60	176.77	M1.5V	9.4	8.0	3.9	5.1	75
GJ 213	05:42:09.26772	+12:29:21.6225	2000.53	-1569.63	171.55	M4.0V	13.1	11.5	6.4	7.6	20
GJ 229	06:10:34.61533	-21:51:52.7117	-137.09	-713.66	173.81	M1/M2V	9.6	8.1	4.2	5.4	25
HIP 31293	06:33:43.29814	-75:37:47.9759	-290.15	277.00	110.88	M2V	11.9	10.3	5.9	6.1	10
HIP 31292	06:33:46.84863	-75:37:30.2972	-291.38	221.24	115.19	M3V	12.9	11.4	6.6	6.9	18
GJ 3404A	06:42:11.193	+03:34:52.63	38.50	-259.30	64.00	M3.5	13.3	11.7	7.3	6.4	15
GJ 3405B	06:42:13.34	+03:35:31.1	35.00	-285.00	64.00	M4	11.6	13.3	8.3	7.3	4
GJ 250B	06:52:18.05	-05:11:24.2	-541.00	0.00	114.80	M2	11.5	10.1	5.7	6.0	13
GJ 273	07:27:24.49975	+05:13:32.8332	572.51	-3693.51	262.98	M3.5V	11.4	9.9	4.9	7.0	169
GJ 3459	07:38:40.95640	-21:13:28.5046	450.28	-477.71	94.31	M3	13.3	11.7	7.1	6.9	8
GJ 285	07:44:40.17401	+03:33:08.8350	-345.25	-450.70	167.88	M4.5V	12.8	11.2	5.7	6.8	7
GJ 299	08:11:57.575	+08:46:22.05	1099.00	-5123.00	148.00	M4.5V	14.6	12.8	7.7	8.5	22
GJ 300	08:12:40.881	-21:33:05.68	9.00	-694.00	125.60	M4	13.7	12.1	6.7	7.2	39
GJ 2066	08:16:07.98235	+01:18:09.2631	-374.45	60.10	109.62	M2.0V	11.6	10.1	5.8	6.0	8
GJ 1123	09:17:05.328	-77:49:23.37	695.00	-866.00	110.90	M4	14.7	13.1	7.4	7.7	7
GJ 341	09:21:37.60463	-60:16:55.0407	-837.79	180.67	95.58	M0.0	11.0	9.5	5.6	5.5	57
GJ 1125	09:30:44.58334	+00:19:21.5651	-571.90	-553.76	103.46	M3.5	13.3	11.7	6.9	6.9	9
GJ 357	09:36:01.63592	-21:39:38.8679	136.67	-989.13	110.82	M2.5V	12.5	10.9	6.5	6.7	53
GJ 358	09:39:46.36930	-41:04:03.2100	-526.56	356.39	105.63	M3	12.2	10.7	6.1	6.2	38

Table D.1. continued.

Name	α (2000)	δ (2000)	μ_α [mas yr^{-1}]	μ_δ [mas yr^{-1}]	π [mas]	Spec. type	B [mag]	V [mag]	K_S [mag]	M_{K_S} [mag]	$N_{\rm spectra}$
GJ 367	09:44:29.83739	-45:46:35.4273	-461.73	-584.28	101.31	M1.0	11.4	10.0	5.8	5.8	24
GJ 1129	09:44:47.315	-18:12:48.93	-1606.00	-172.00	90.90	M4	14.2	12.6	7.3	7.0	8
GJ 382	10:12:17.66904	-03:44:44.3966	-151.09	-244.31	127.08	M2.0V	10.8	9.3	5.0	5.5	33
GJ 388	10:19:36.277	+19:52:12.06	-501.80	-42.80	213.00	M4.5Ve	9.6	8.1	4.6	6.2	43
GJ 393	10:28:55.55087	+00:50:27.6218	-603.75	-728.94	141.50	M2.5V	11.2	9.7	5.3	6.1	29
GJ 3618	10:44:21.320	-61:12:38.44	-334.00	1626.00	208.95	M4	15.7	13.9	7.7	9.3	7
GJ 402	10:50:52.03129	+06:48:29.2278	-855.92	-822.34	147.92	M5.0V	13.3	11.7	6.4	7.2	6
GJ 406	10:56:28.865	+07:00:52.77	-3842.00	-2725.00	418.30	M6.0V	15.5	13.5	6.1	9.2	29
GJ 413.1	11:09:31.34559	-24:35:55.1194	-796.18	-446.82	93.00	M2	12.0	10.4	6.1	5.9	18
GJ 433	11:35:26.94663	-32:32:23.8952	-72.51	-851.92	112.58	M1.5	11.3	9.8	5.6	5.9	86
GJ 436	11:42:11.094	+26:42:23.65	896.07	-813.54	99.00	M3.5V	12.1	10.6	6.1	6.1	169
GJ 438	11:43:19.811	-51:50:25.98	654.10	-538.50	118.90	M0	11.9	10.3	6.3	6.7	19
GJ 447	11:47:44.405	+00:48:16.44	605.26	-1219.28	298.04	M4.5V	12.9	11.2	5.7	8.0	41
GJ 465	12:24:52.50278	-18:14:32.2435	1095.66	-2308.56	112.98	M2	12.9	11.3	7.0	7.2	24
GJ 479	12:37:52.21838	-52:00:05.3142	-1032.41	30.39	103.18	M3Ve	12.2	10.7	6.0	6.1	58
GJ 3737	12:38:49.141	-38:22:52.80	-567.00	-1399.00	156.78	M4.5V	14.4	12.7	7.4	8.4	10
GJ 480.1	12:40:46.28898	-43:33:58.9535	-781.58	693.43	128.52	M3V	14.0	12.2	7.4	8.0	10
GJ 486	12:47:56.62550	+09:45:05.0355	-1006.76	-460.19	119.47	M4.0V	13.0	11.4	6.4	6.7	12
GJ 514	13:29:59.78622	+10:22:37.7908	1128.32	-1073.47	130.62	M1.0V	10.5	9.0	5.0	5.6	57
GJ 526	13:45:43.77665	+14:53:29.4635	1778.45	-1456.44	185.49	M4.0V	9.9	8.5	4.4	5.8	31
GJ 536	14:01:03.18912	-02:39:17.5212	-823.47	598.19	99.72	M1.5V	11.2	9.7	5.7	5.7	52
GJ 551	14:29:42.94853	-62:40:46.1631	-3775.75	765.54	771.64	M6Ve	12.9	11.1	4.4	8.8	261
GJ 555	14:34:16.81183	-12:31:10.3965	-354.45	595.35	164.99	M4.0V	12.9	11.3	5.9	7.0	14
GJ 569A	14:54:29.241	+16:06:03.76	277.70	-132.70	101.90	M2.5V	12.3	10.4	...	...	25
GJ 581	15:19:26.823	-07:43:20.21	-1227.67	-97.78	160.91	M5.0V	11.8	10.6	5.8	6.9	243
GJ 588	15:32:12.93186	-41:16:32.1081	-1177.12	-1028.54	168.66	M2.5V	10.8	9.3	4.8	5.9	255
GJ 618A	16:20:03.509	-37:31:44.80	-740.10	997.40	119.80	M3	12.1	10.6	6.0	6.3	21
GJ 628	16:30:18.05803	-12:39:45.3232	-94.81	-1183.43	232.98	M3V	11.6	10.1	5.1	6.9	88
GJ 643	16:55:25.272	-08:19:20.78	-813.83	-894.40	148.92	M3.5V	13.4	11.8	6.7	7.6	10
GJ 667C	17:18:58.838	-34:59:48.64	1155.00	-214.40	146.30	M1.5V	11.8	10.2	6.0	6.9	182
GJ 674	17:28:39.94461	-46:53:42.6930	571.26	-880.83	220.24	M3V	11.0	9.4	4.9	6.6	93
GJ 678.1A	17:30:22.727	+05:32:54.71	29.13	-248.15	100.20	M1V	10.8	9.3	5.4	5.4	75
GJ 680	17:35:13.61562	-48:40:51.1341	82.62	454.25	102.83	M3V	11.7	10.1	5.8	5.9	39
GJ 682	17:37:03.66242	-44:19:09.1697	-708.98	-937.40	196.90	M3.5	12.6	10.9	5.6	7.1	21
GJ 686	17:37:53.34690	+18:35:30.1613	926.78	984.20	123.67	M1.0V	11.1	9.6	5.6	6.0	20
GJ 693	17:46:34.22971	-57:19:08.5550	-1119.14	-1352.78	171.48	M2.0	12.4	10.8	6.0	7.2	54
GJ 699	17:57:48.49803	+04:41:36.2072	-798.58	10328.12	548.31	M4.0V	11.2	9.5	4.5	8.2	234
GJ 701	18:05:07.57896	-03:01:52.7575	570.26	-333.47	128.89	M2.0V	10.9	9.4	5.3	5.9	63
GJ 1224	18:07:32.927	-15:57:46.46	-617.00	-342.00	132.60	M4.5V	15.4	13.6	7.8	8.4	9
GJ 4071	18:42:44.99	+13:54:16.8	-25.00	347.00	93.30	M4.5	14.8	12.8	7.6	7.4	5
GJ 729	18:49:49.36216	-23:50:10.4291	637.02	-191.64	336.72	M3Ve	12.2	10.5	5.4	8.0	8
GJ 1232	19:09:50.980	+17:40:07.45	-637.00	-426.00	93.60	M4.5	15.4	13.6	7.9	7.8	9
GJ 752A	19:16:55.25687	+05:10:08.0510	-578.78	-1331.95	170.36	M3V	10.6	9.1	4.7	5.8	57

Table D.1. continued.

Name	α (2000)	δ (2000)	μ_α [mas yr^{-1}]	μ_δ [mas yr^{-1}]	π [mas]	Spec. type	B [mag]	V [mag]	K_S [mag]	M_{K_S} [mag]	$N_{\rm spectra}$
GJ 754	19:20:47.955	-45:33:28.33	792.00	-3008.00	169.00	M4.5	13.9	12.2	6.8	8.0	57
GJ 1236	19:22:02.07	+07:02:31.0	-747.00	-440.00	92.90	M3	14.0	12.3	7.7	7.5	12
GJ 1256	20:40:33.64	+15:29:57.2	1324.00	660.00	100.80	M4.5	15.1	13.4	7.8	7.8	10
GJ 803	20:45:09.53147	-31:20:27.2425	279.96	-360.61	100.91	M1Ve	10.1	8.6	4.5	4.5	4
GJ 4154	20:46:37.26	-81:43:14.1	637.00	-577.00	77.10	M2.5	13.3	···	6.8	6.3	8
LP 816-60	20:52:33.01679	-16:58:29.0249	-307.74	34.79	175.03	M4V	13.0	11.5	6.2	7.4	14
GJ 832	21:33:33.97533	-49:00:32.4192	-46.05	-817.63	201.87	M1.5	10.2	8.7	4.5	6.0	61
GJ 846	22:02:10.27388	+01:24:00.8292	-454.53	-279.09	97.61	M0	10.6	9.1	5.3	5.3	55
GJ 4248	22:02:29.353	-37:04:51.22	910.00	-337.00	134.29	M3.5	13.4	11.8	6.7	7.4	5
GJ 849	22:09:40.34327	-04:38:26.6210	1130.27	-19.27	109.94	M3.5V	11.9	10.4	5.6	5.8	48
GJ 1265	22:13:42.78	-17:41:08.2	849.00	-302.00	96.00	M4	15.3	13.6	8.1	8.0	13
GJ 4274	22:23:06.97	-17:36:25.0	248.00	-895.00	134.10	M4	15.1	13.2	7.3	8.0	4
GJ 876	22:53:16.73352	-14:15:49.3186	959.84	-675.33	213.28	M5.0V	11.7	10.2	5.0	6.7	196
GJ 877	22:55:45.50948	-75:27:31.2069	-1027.76	-1060.78	116.07	M3V	11.9	10.4	5.8	6.1	46
GJ 880	22:56:34.80475	+16:33:12.3541	-1034.34	-284.09	146.09	M2.0V	10.1	8.6	4.5	5.3	36
GJ 887	23:05:52.03604	-35:51:11.0475	6768.20	1327.52	305.26	M2V	8.8	7.3	3.5	5.9	77
GJ 4333	23:21:37.44994	+17:17:25.3922	-534.13	-1382.74	91.00	M4	13.2	11.7	6.5	6.3	7
GJ 908	23:49:12.52790	+02:24:04.4072	996.96	-967.88	167.29	M2V	10.4	9.0	5.0	6.2	83
LTT 9759	23:53:50.11043	-75:37:57.1048	243.04	-378.12	100.07	Ma	11.5	10.0	5.5	5.6	11
GJ 676A	17:30:11.20344	-51:38:13.1046	-260.02	-184.29	60.79	M0V	11.0	9.6	5.8	4.7	123
GJ 1214	17:15:18.94	+04:57:49.7	585.00	-752.00	77.20	M4.5V	16.4	14.7	8.8	8.2	88
HIP 12961	02:46:42.88581	-23:05:11.8047	292.62	140.88	43.45	M0	11.7	10.2	6.7	4.9	48
GJ 163	04:09:15.66350	-53:22:25.3050	1041.43	583.01	66.69	M3.5	13.3	11.8	7.1	6.3	170
GJ 317	08:40:59.24	-23:27:23.3	-438.00	794.00	65.30	M3.5V	13.2	12.0	7.0	6.1	80
GJ 570B	14:57:26.53330	-21:24:41.5778	961.78	-1677.83	168.77	M1.5V	9.6	8.1	3.8	4.9	347
GJ 160.2	04:06:34.84136	-20:51:11.2391	51.90	-780.04	43.25	K7	10.9	9.7	6.7	4.9	37
GJ 180	04:53:49.97976	-17:46:24.2944	408.07	-642.82	82.52	M2	12.4	10.9	6.6	6.2	77
GJ 3634	10:58:35.133	-31:08:38.29	-583.00	-92.00	50.55	M2.5	14.4	11.9	7.5	6.0	77
GJ 3470	07:59:05.87	+15:23:29.5	-175.00	-52.00	39.68	M1.5	13.5	12.3	8.0	6.0	98

Table D.2. Stellar parameters

Name	$T_{\rm eff,\,SpT}$ [K]	$T_{\rm eff,\,\mathcal{M}_\star}$ [K]	$T_{\rm eff,\,M15}$ [K]	[Fe/H]	[Fe/H] source
GJ 1	3650	3546	3482	-0.45	1
GJ 1002	3070	2536	...	-0.27	1
GJ 12	3470	3333	...	-0.29	1
GJ 3049	3470	3253	...	-0.13	1
GJ 54.1	3370	2916	...	-0.38	1
L 707-74	...	3021	...	-0.38	1
GJ 87	3520	3641	3562	-0.32	1
GJ 105B	3310	3413	...	-0.02	1
CD-44-836A	3370	3304	...	-0.07	1
CD-44-836B	3200	3183	...	...	...
GJ 3189	3470	3113	...	-0.76	1
GJ 3193B	3470	3491	...	-0.34	1
GJ 3207	3420	...	...	...	...
GJ 1057	3200	3074	...	-0.10	1
GJ 145	3520	3471	...	-0.28	1
GJ 1061	3070	2752	...	-0.09	1
GJ 1065	3470	3226	...	-0.23	1
GJ 1068	3310	2849	...	-0.43	1
GJ 166C	3200	3328	...	-0.12	1
GJ 176	3520	3713	3603	-0.01	1
GJ 3323	3370	3110	...	-0.24	1
GJ 3325	3470	3419	...	-0.19	1
GJ 191	3720	3423	3587	-0.85	1
GJ 203	3420	3231	...	-0.22	1
GJ 205	3650	...	3800	0.19	1
GJ 213	3370	3301	...	-0.11	1
GJ 229	3650	...	3779	-0.03	1
HIP 31293	3580	3615	3526	-0.05	1
HIP 31292	3470	3454	...	-0.06	1
GJ 3404A	3420	3542	...	-0.02	1
GJ 3405B	3370	3360	...	...	...
GJ 250B	3580	3632	3557	-0.08	1
GJ 273	3420	3441	3342	-0.01	1
GJ 3459	3470	3444	...	-0.22	1
GJ 285	3310	3461	...	0.27	1
GJ 299	3310	2942	...	-0.53	1
GJ 300	3370	3392	...	0.13	1
GJ 2066	3580	3647	3575	-0.17	1
GJ 1123	3310	3269	...	0.15	1
GJ 341	3850	...	3783	-0.14	1
GJ 1125	3420	3443	...	-0.09	1
GJ 357	3520	3480	3477	-0.30	1
GJ 358	3470	3592	3450	-0.01	1
GJ 367	3720	3700	3559	-0.07	1
GJ 1129	3370	3429	...	0.05	1
GJ 382	3580	...	3653	0.02	1
GJ 388	3310	3576	3473	0.12	1
GJ 393	3520	3620	3544	-0.20	1
GJ 3618	3370	...	...	-0.55	1
GJ 402	3200	3385	...	0.03	1
GJ 406	2900	2509	...	0.19	1
GJ 413.1	3580	3655	3570	-0.10	1
GJ 433	3650	3675	3618	-0.17	1
GJ 436	3420	3624	...	...	...
GJ 438	3850	3480	3647	-0.36	1
GJ 447	3310	3152	3382	-0.17	1
GJ 465	3580	3387	3403	-0.62	1
GJ 479	3470	3614	3476	0.01	1
GJ 3737	3310	2997	...	-0.27	1

Table D.2. continued.

Name	$T_{\rm eff,\,SpT}$ [K]	$T_{\rm eff,\,\mathcal{M}_\star}$ [K]	$T_{\rm eff,\,M15}$ [K]	[Fe/H]	[Fe/H] source
GJ 480.1	3470	3190	...	-0.48	1
GJ 486	3370	3472	...	0.03	1
GJ 514	3720	3812	3728	-0.16	1
GJ 526	3370	3718	3609	-0.22	1
GJ 536	3650	3773	3685	-0.14	1
GJ 551	2900	2718	3555	0.16	1
GJ 555	3370	3432	...	0.14	1
GJ 569A	3520	...	3608	-0.06	1
GJ 581	3200	3454	3419	-0.20	1
GJ 588	3520	3670	3525	0.06	1
GJ 618A	3470	3548	3451	-0.06	1
GJ 628	3470	3448	3345	-0.02	1
GJ 643	3420	3293	...	-0.26	1
GJ 644A	...	...	3463	...	...
GJ 667C	3650	3455	...	-0.50	1
GJ 674	3470	3500	3484	-0.23	1
GJ 678.1A	3720	...	3815	-0.14	1
GJ 680	3470	3672	3585	-0.19	1
GJ 682	3420	3425	3393	0.10	1
GJ 686	3720	3629	3677	-0.35	1
GJ 693	3580	3396	3390	-0.28	1
GJ 699	3370	3055	...	-0.51	1
GJ 701	3580	3683	3664	-0.27	1
GJ 1224	3310	2967	...	-0.25	1
GJ 4071	3310	3339	...	-0.08	1
GJ 729	3470	3163	3548	-0.40	1
GJ 1232	3310	3246	...	0.03	1
GJ 752A	3470	3692	3551	0.05	1
GJ 754	3310	3175	...	-0.14	1
GJ 1236	3470	3311	...	-0.47	1
GJ 1256	3310	3244	...	0.06	1
GJ 803	3720	...	...	...	...
GJ 4154	3520	3569	...	-0.22	1
LP 816-60	3370	3336	...	-0.07	1
GJ 832	3650	3631	3580	-0.17	1
GJ 846	3850	...	3835	0.01	1
GJ 4248	3420	3349	...	-0.13	1
GJ 849	3420	3703	3486	0.22	1
GJ 1265	3370	3152	...	-0.20	1
GJ 4274	3370	3191	...	0.10	1
GJ 876	3200	3486	3357	0.14	1
GJ 877	3470	3602	3428	0.00	1
GJ 880	3580	...	3736	0.03	1
GJ 887	3580	3674	3712	-0.24	1
GJ 4333	3370	3558	...	0.23	1
GJ 908	3580	3595	3570	-0.44	1
LTT 9759	...	...	3581	0.17	1
GJ 676A	3850	...	...	0.26	1
GJ 1214	3310	3055	...	0.05	1
HIP 12961	3850	...	...	0.22	1
GJ 163	3420	3571	...	0.07	1
GJ 317	3420	3610	...	0.22	1
GJ 570B	3650	...	...	0.29	2
GJ 160.2	3850	...	...	...	...
GJ 180	3580	3590	...	-0.20	2
GJ 3634	3520	3641	...	-0.07	1
GJ 3470	3650	3642	...	...	...

References. (1) Neves et al. (2014); (2) Neves et al. (2012).

Table D.3. Results

Name	$R'_{\rm HK}{}^{a}$ $\left(T_{\rm eff,SpT}\right)$	$R'_{\rm HK}{}^{a}$ $(T_{\rm eff,\mathcal{M}_\star})$	$R'_{\rm HK}{}^{a}$ $(T_{\rm eff,M15})$	$\mathcal{F}'_{\rm H\alpha}/\mathcal{F}_{\rm bol}$ $\left(T_{\rm eff,SpT}\right)$	$\mathcal{F}'_{\rm H\alpha}/\mathcal{F}_{\rm bol}$ $(T_{\rm eff,\mathcal{M}_\star})$	$\mathcal{F}'_{\rm H\alpha}/\mathcal{F}_{\rm bol}$ $(T_{\rm eff,M15})$
GJ 1	-5.46	-5.54	-5.60	-1.95e-05	-1.87e-05	-1.82e-05
GJ 1002	-5.31	-6.62	...	-6.77e-06	-1.57e-06	...
GJ 12	-5.22	-5.35	...	-1.49e-05	-1.36e-05	...
GJ 3049	-5.22	-5.43	...	-1.03e-05	-8.71e-06	...
GJ 54.1	-4.36	-5.05	...	6.23e-05	2.63e-05	...
L 707-74	...	-5.86	...	...	-1.00e-05	...
GJ 87	-5.28	-5.19	-5.24	-2.30e-05	-2.41e-05	-2.34e-05
GJ 105B	-5.41	-5.31	...	-1.21e-05	-1.38e-05	...
CD-44-836A	-4.57	-4.63	...	5.03e-05	4.58e-05	...
CD-44-836B	-4.76	-4.78	...	1.82e-04	1.77e-04	...
GJ 3189	-5.54	-6.13	...	-1.52e-05	-1.41e-05	...
GJ 3193B	-5.40	-5.38	...	-1.53e-05	-1.54e-05	...
GJ 3207	...	...	...	...	...	...
GJ 1057	-5.04	-5.21	...	-1.06e-07	-3.98e-07	...
GJ 145	-4.92	-4.96	...	-9.62e-06	-9.40e-06	...
GJ 1061	-5.17	-5.81	...	-3.90e-06	-1.37e-06	...
GJ 1065	-5.16	-5.42	...	-1.05e-05	-9.35e-06	...
GJ 1068	-5.32	-6.16	...	-7.39e-06	-4.93e-06	...
GJ 166C	-4.41	-4.28	...	1.40e-04	1.71e-04	...
GJ 176	-4.78	-4.68	-4.74	-1.59e-05	-1.78e-05	-1.69e-05
GJ 3323	-4.50	-4.80	...	5.19e-05	3.47e-05	...
GJ 3325	-5.14	-5.18	...	-1.54e-05	-1.47e-05	...
GJ 191	-5.61	-5.96	-5.74	-1.91e-05	-1.93e-05	-1.92e-05
GJ 203	-5.34	-5.56	...	-1.05e-05	-8.89e-06	...
GJ 205	-4.59	...	-4.53	-2.28e-05	...	-2.55e-05
GJ 213	-5.54	-5.62	...	-1.30e-05	-1.19e-05	...
GJ 229	-4.70	...	-4.63	-2.86e-05	...	-3.07e-05
HIP 31293	-4.89	-4.87	-4.92	-1.46e-05	-1.49e-05	-1.41e-05
HIP 31292	-5.11	-5.12	...	-1.44e-05	-1.42e-05	...
GJ 3404A	-5.37	-5.28	...	-1.38e-05	-1.60e-05	...
GJ 3405B	-5.64	-5.65	...	-6.29e-05	-6.22e-05	...
GJ 250B	-4.91	-4.88	-4.92	-1.99e-05	-2.05e-05	-1.95e-05
GJ 273	-5.28	-5.26	-5.34	-1.46e-05	-1.50e-05	-1.33e-05
GJ 3459	-5.20	-5.22	...	-1.52e-05	-1.50e-05	...
GJ 285	-3.83	-3.74	...	3.33e-04	4.06e-04	...
GJ 299	-5.39	-6.08	...	-1.24e-05	-8.42e-06	...
GJ 300	-5.01	-4.99	...	-6.76e-06	-6.93e-06	...
GJ 2066	-5.09	-5.05	-5.09	-2.22e-05	-2.34e-05	-2.22e-05
GJ 1123	-4.95	-4.98	...	-8.16e-06	-7.66e-06	...
GJ 341	-4.67	...	-4.71	-3.03e-05	...	-2.98e-05
GJ 1125	-5.38	-5.37	...	-1.25e-05	-1.29e-05	...
GJ 357	-5.53	-5.56	-5.57	-1.75e-05	-1.72e-05	-1.72e-05
GJ 358	-4.50	-4.43	-4.51	4.13e-05	4.71e-05	4.03e-05
GJ 367	-4.91	-4.92	-4.99	-2.43e-05	-2.41e-05	-2.18e-05
GJ 1129	-5.08	-5.03	...	-1.09e-05	-1.17e-05	...
GJ 382	-4.63	...	-4.60	-1.79e-05	...	-1.87e-05
GJ 388	-4.17	-4.01	-4.06	1.42e-04	1.98e-04	1.76e-04
GJ 393	-4.99	-4.92	-4.97	-1.83e-05	-1.93e-05	-1.86e-05
GJ 3618	-5.32	...	...	-1.25e-05	...	...
GJ 402	-5.29	-5.10	...	-6.54e-06	-8.18e-06	...
GJ 406	-4.10	-4.97	...	1.52e-04	4.66e-05	...
GJ 413.1	-5.08	-5.04	-5.09	-2.30e-05	-2.42e-05	-2.29e-05
GJ 433	-5.06	-5.05	-5.08	-2.56e-05	-2.60e-05	-2.52e-05
GJ 436	-5.36	-5.23	...	-1.62e-05	-1.95e-05	...
GJ 438	-5.06	-5.32	-5.19	-2.55e-05	-2.28e-05	-2.47e-05
GJ 447	-5.26	-5.45	-5.19	-9.74e-06	-8.65e-06	-1.01e-05
GJ 465	-5.80	-6.07	-6.04	-2.51e-05	-2.30e-05	-2.31e-05
GJ 479	-4.68	-4.60	-4.68	5.42e-06	7.00e-06	5.47e-06
GJ 3737	-5.40	-5.92	...	-1.07e-05	-7.74e-06	...

Table D.3. continued.

Name	$R'_{\rm HK}{}^{a}$ $\left(T_{\rm eff,SpT}\right)$	$R'_{\rm HK}{}^{a}$ $(T_{\rm eff,\mathcal{M}_\star})$	$R'_{\rm HK}{}^{a}$ $(T_{\rm eff,M15})$	$\mathcal{F}'_{\rm H\alpha}/\mathcal{F}_{\rm bol}$ $\left(T_{\rm eff,SpT}\right)$	$\mathcal{F}'_{\rm H\alpha}/\mathcal{F}_{\rm bol}$ $(T_{\rm eff,\mathcal{M}_\star})$	$\mathcal{F}'_{\rm H\alpha}/\mathcal{F}_{\rm bol}$ $(T_{\rm eff,M15})$
GJ 480.1	-5.17	-5.52	...	-1.28e-05	-1.19e-05	...
GJ 486	-5.47	-5.38	...	-1.16e-05	-1.29e-05	...
GJ 514	-4.86	-4.82	-4.86	-3.10e-05	-3.20e-05	-3.11e-05
GJ 526	-5.28	-5.03	-5.09	-2.27e-05	-2.86e-05	-2.72e-05
GJ 536	-4.88	-4.82	-4.86	-3.00e-05	-3.17e-05	-3.05e-05
GJ 551	-4.59	-5.01	-3.92	4.34e-05	2.39e-05	1.41e-04
GJ 555	-5.23	-5.19	...	-7.31e-06	-7.81e-06	...
GJ 569A	-4.27	...	-4.22	5.44e-05	...	5.98e-05
GJ 581	-5.96	-5.61	-5.64	-1.10e-05	-1.29e-05	-1.26e-05
GJ 588	-5.07	-5.00	-5.06	-1.71e-05	-1.92e-05	-1.72e-05
GJ 618A	-5.23	-5.18	-5.25	-1.93e-05	-2.08e-05	-1.89e-05
GJ 628	-5.27	-5.29	-5.37	-1.28e-05	-1.25e-05	-1.12e-05
GJ 643	-5.43	-5.57	...	-1.20e-05	-1.13e-05	...
GJ 667C	-5.33	-5.50	...	-2.00e-05	-1.89e-05	...
GJ 674	-4.84	-4.82	-4.83	4.42e-06	4.69e-06	4.55e-06
GJ 678.1A	-4.76	...	-4.71	-3.07e-05	...	-3.18e-05
GJ 680	-5.12	-5.00	-5.05	-2.30e-05	-2.63e-05	-2.51e-05
GJ 682	-5.17	-5.16	-5.18	-9.35e-06	-9.41e-06	-9.01e-06
GJ 686	-5.14	-5.19	-5.16	-2.60e-05	-2.53e-05	-2.57e-05
GJ 693	-5.47	-5.63	-5.64	-1.61e-05	-1.45e-05	-1.44e-05
GJ 699	-5.56	-6.12	...	-1.35e-05	-1.20e-05	...
GJ 701	-5.00	-4.94	-4.95	-2.81e-05	-2.98e-05	-2.96e-05
GJ 1224	-4.20	-4.67	...	1.99e-04	1.03e-04	...
GJ 4071	-4.22	-4.19	...	1.86e-04	1.94e-04	...
GJ 729	-4.17	-4.50	-4.10	1.51e-04	1.02e-04	1.61e-04
GJ 1232	-5.15	-5.21	...	-5.02e-06	-4.75e-06	...
GJ 752A	-5.01	-4.90	-4.96	-1.60e-05	-1.93e-05	-1.74e-05
GJ 754	-5.26	-5.43	...	-9.27e-06	-8.22e-06	...
GJ 1236	-5.24	-5.42	...	-1.30e-05	-1.24e-05	...
GJ 1256	-4.82	-4.89	...	7.36e-06	6.56e-06	...
GJ 803	...	...	...	...	...	...
GJ 4154	-5.04	-5.01	...	-1.29e-05	-1.31e-05	...
LP 816-60	-5.08	-5.11	...	-8.99e-06	-8.72e-06	...
GJ 832	-5.10	-5.11	-5.14	-2.55e-05	-2.52e-05	-2.43e-05
GJ 846	-4.56	...	-4.56	-3.18e-05	...	-3.17e-05
GJ 4248	-5.26	-5.32	...	-1.30e-05	-1.22e-05	...
GJ 849	-5.10	-4.98	-5.06	-1.73e-05	-2.32e-05	-1.87e-05
GJ 1265	-5.19	-5.45	...	-6.82e-06	-6.03e-06	...
GJ 4274	-4.27	-4.43	...	1.85e-04	1.41e-04	...
GJ 876	-5.40	-5.15	-5.23	-7.74e-06	-1.14e-05	-9.78e-06
GJ 877	-5.21	-5.14	-5.24	-1.65e-05	-1.92e-05	-1.57e-05
GJ 880	-4.77	...	-4.69	-2.74e-05	...	-3.06e-05
GJ 887	-4.91	-4.85	-4.83	-2.56e-05	-2.70e-05	-2.75e-05
GJ 4333	-5.01	-4.91	...	-5.48e-06	-6.58e-06	...
GJ 908	-5.39	-5.37	-5.39	-2.45e-05	-2.46e-05	-2.44e-05
LTT 9759	...	...	-4.77	...	...	-1.97e-05
GJ 676A	-4.67	...	...	-3.66e-05	...	...
GJ 1214	-5.07	-5.39	...	-9.69e-06	-6.01e-06	...
HIP 12961	-4.56	...	...	-3.69e-05	...	...
GJ 163	-5.29	-5.20	...	-1.59e-05	-1.92e-05	...
GJ 317	-5.05	-4.96	...	-9.09e-06	-1.19e-05	...
GJ 570B	-4.79	...	...	-2.39e-05	...	...
GJ 160.2	-4.93	...	...	-5.73e-05	...	...
GJ 180	-5.11	-5.11	...	-2.00e-05	-2.01e-05	...
GJ 3634	-5.06	-4.99	...	-2.23e-05	-2.44e-05	...
GJ 3470	-4.72	-4.73	...	-2.03e-05	-2.02e-05	...

Notes. [(a)] Values are on a log scale.

Table D.4. PHOENIX-ACES grid calibrations

[Fe/H]		-1.00		-0.50		0.00		+0.50		+1.00	
$T_{\rm eff}$	$\log g$	log	log	log	log	log	log	log	log	log	log
[K]		$C_{\rm cf}$	$R_{\rm HK,\,phot}$	$C_{\rm cf}$	$R_{\rm HK,\,phot}$	$C_{\rm cf}$	$R_{\rm HK,\,phot}$	$C_{\rm cf}$	$R_{\rm HK,\,phot}$	$C_{\rm cf}$	$R_{\rm HK,\,phot}$
2300	4.0	-2.95	-7.63	-2.65	-7.27	-2.34	-6.86	-2.13	-6.50	-2.00	-6.26
2400	4.0	-2.68	-7.34	-2.40	-6.97	-2.14	-6.61	-1.96	-6.31	-1.86	-6.13
2500	4.0	-2.42	-7.04	-2.17	-6.69	-1.96	-6.40	-1.81	-6.16	-1.73	-6.03
2600	4.0	-2.26	-6.82	-2.01	-6.52	-1.80	-6.24	-1.67	-6.06	-1.61	-5.96
2700	4.0	-2.04	-6.61	-1.83	-6.34	-1.66	-6.12	-1.55	-5.98	-1.50	-5.91
2800	4.0	-1.86	-6.43	-1.68	-6.21	-1.53	-6.02	-1.44	-5.92	-1.40	-5.88
2900	4.0	-1.69	-6.30	-1.54	-6.10	-1.42	-5.96	-1.34	-5.89	-1.31	-5.87
3000	4.0	-1.55	-6.19	-1.42	-6.03	-1.31	-5.92	-1.24	-5.88	-1.24	-5.88
3100	4.0	-1.42	-6.11	-1.31	-5.99	-1.22	-5.91	-1.17	-5.89	-1.17	-5.90
3200	4.0	-1.30	-6.05	-1.21	-5.96	-1.14	-5.92	-1.10	-5.91	-1.12	-5.93
3300	4.0	-1.20	-6.01	-1.13	-5.96	-1.07	-5.94	-1.05	-5.95	-1.06	-5.98
3400	4.0	-1.10	-5.97	-1.06	-5.93	-1.02	-5.95	-1.00	-5.99	-1.01	-6.02
3500	4.0	-1.01	-5.92	-0.99	-5.88	-0.97	-5.91	-0.97	-5.99	-0.99	-6.04
3600	4.0	-0.93	-5.85	-0.93	-5.82	-0.94	-5.86	-0.94	-5.95	-0.96	-6.01
3700	4.0	-0.86	-5.74	-0.88	-5.77	-0.90	-5.81	-0.91	-5.88	-0.92	-5.96
3800	4.0	-0.79	-5.62	-0.82	-5.73	-0.85	-5.78	-0.87	-5.82	-0.89	-5.85
3900	4.0	-0.72	-5.54	-0.76	-5.70	-0.80	-5.74	-0.83	-5.77	-0.85	-5.79
4000	4.0	-0.65	-5.46	-0.70	-5.66	-0.74	-5.72	-0.78	-5.75	-0.82	-5.75
4100	4.0	-0.58	-5.45	-0.63	-5.63	-0.68	-5.69	-0.73	-5.72	-0.78	-5.73
4200	4.0	-0.51	-5.40	-0.56	-5.60	-0.61	-5.67	-0.67	-5.70	-0.73	-5.72
4300	4.0	-0.44	-5.38	-0.48	-5.54	-0.55	-5.63	-0.61	-5.69	-0.68	-5.71
4400	4.0	-0.37	-5.30	-0.42	-5.46	-0.48	-5.58	-0.55	-5.66	-0.63	-5.70
4500	4.0	-0.31	-5.21	-0.35	-5.38	-0.42	-5.51	-0.49	-5.62	-0.58	-5.68
4600	4.0	-0.26	-5.13	-0.30	-5.29	-0.36	-5.44	-0.43	-5.55	-0.52	-5.65
4700	4.0	-0.21	-5.05	-0.25	-5.22	-0.30	-5.36	-0.38	-5.48	-0.46	-5.61
4800	4.0	-0.17	-4.98	-0.20	-5.14	-0.25	-5.28	-0.32	-5.40	-0.41	-5.55
4900	4.0	-0.12	-4.91	-0.16	-5.06	-0.21	-5.19	-0.27	-5.31	-0.37	-5.47
5000	4.0	-0.08	-4.82	-0.11	-4.99	-0.16	-5.11	-0.23	-5.23	-0.31	-5.41
5100	4.0	-0.06	-4.62	-0.09	-4.71	-0.13	-4.75	-0.19	-4.76	-0.27	-4.76
5200	4.0	-0.03	-4.59	-0.05	-4.63	-0.09	-4.70	-0.15	-4.70	-0.23	-4.67
5300	4.0	0.00	-4.53	-0.02	-4.60	-0.05	-4.64	-0.11	-4.65	-0.18	-4.62
5400	4.0	0.03	-4.49	0.02	-4.55	-0.02	-4.60	-0.07	-4.60	-0.14	-4.57
5500	4.0	0.06	-4.45	0.04	-4.51	0.01	-4.55	-0.03	-4.55	-0.11	-4.52
5600	4.0	0.08	-4.42	0.06	-4.48	0.05	-4.51	-0.02	-4.52	-0.09	-4.50
5700	4.0	0.11	-4.38	0.10	-4.44	0.07	-4.47	0.01	-4.47	-0.05	-4.46
5800	4.0	0.13	-4.35	0.11	-4.41	0.10	-4.44	0.05	-4.44	-0.02	-4.42
5900	4.0	0.15	-4.32	0.14	-4.38	0.12	-4.41	0.07	-4.41	0.01	-4.40
6000	4.0	0.17	-4.28	0.15	-4.34	0.15	-4.38	0.10	-4.38	0.04	-4.35
6100	4.0	0.19	-4.25	0.17	-4.32	0.16	-4.36	0.13	-4.35	0.06	-4.33
6200	4.0	0.21	-4.22	0.21	-4.29	0.19	-4.33	0.15	-4.33	0.10	-4.30
6300	4.0	0.22	-4.18	0.23	-4.26	0.21	-4.30	0.18	-4.30	0.12	-4.28
6400	4.0	0.25	-4.16	0.24	-4.23	0.23	-4.27	0.19	-4.28	0.15	-4.25
6500	4.0	0.26	-4.13	0.26	-4.19	0.25	-4.25	0.22	-4.26	0.17	-4.23
6600	4.0	0.28	-4.09	0.27	-4.16	0.26	-4.21	0.24	-4.23	0.19	-4.21
6700	4.0	0.29	-4.06	0.29	-4.13	0.28	-4.19	0.25	-4.20	0.21	-4.19
6800	4.0	0.30	-4.03	0.30	-4.10	0.29	-4.16	0.27	-4.18	0.22	-4.17
6900	4.0	0.31	-3.99	0.31	-4.06	0.30	-4.13	0.29	-4.15	0.23	-4.15
7000	4.0	0.32	-3.96	0.32	-4.03	0.32	-4.10	0.30	-4.12	0.25	-4.13
7200	4.0	0.34	-3.89	0.34	-3.97	0.34	-4.03	0.33	-4.06	0.29	-4.07
2300	4.5	-3.26	-7.86	-2.92	-7.53	-2.56	-7.15	-2.27	-6.73	-2.08	-6.41
2400	4.5	-2.94	-7.60	-2.65	-7.28	-2.33	-6.89	-2.08	-6.50	-1.92	-6.22
2500	4.5	-2.66	-7.32	-2.40	-6.99	-2.13	-6.64	-1.91	-6.29	-1.78	-6.07
2600	4.5	-2.50	-7.04	-2.15	-6.70	-1.94	-6.42	-1.76	-6.13	-1.65	-5.96
2700	4.5	-2.26	-6.80	-2.01	-6.54	-1.78	-6.23	-1.62	-6.01	-1.53	-5.87
2800	4.5	-2.04	-6.58	-1.82	-6.34	-1.63	-6.09	-1.49	-5.92	-1.42	-5.81
2900	4.5	-1.84	-6.42	-1.66	-6.20	-1.50	-5.99	-1.38	-5.85	-1.31	-5.77
3000	4.5	-1.67	-6.28	-1.51	-6.08	-1.37	-5.91	-1.28	-5.80	-1.22	-5.75
3100	4.5	-1.52	-6.16	-1.39	-5.99	-1.27	-5.86	-1.19	-5.78	-1.15	-5.75

Table D.4. continued.

[Fe/H]		-1.00		-0.50		0.00		+0.50		+1.00	
$T_{\rm eff}$ [K]	$\log g$	log $C_{\rm cf}$	log $R_{\rm HK,\,phot}$	log $C_{\rm cf}$	log $R_{\rm HK,\,phot}$	log $C_{\rm cf}$	log $R_{\rm HK,\,phot}$	log $C_{\rm cf}$	log $R_{\rm HK,\,phot}$	log $C_{\rm cf}$	log $R_{\rm HK,\,phot}$
3200	4.5	-1.38	-6.06	-1.28	-5.93	-1.18	-5.83	-1.11	-5.77	-1.08	-5.76
3300	4.5	-1.26	-5.99	-1.18	-5.88	-1.10	-5.82	-1.04	-5.79	-1.03	-5.79
3400	4.5	-1.15	-5.93	-1.09	-5.84	-1.03	-5.81	-0.99	-5.82	-0.98	-5.83
3500	4.5	-1.05	-5.87	-1.01	-5.79	-0.97	-5.78	-0.95	-5.82	-0.94	-5.86
3600	4.5	-0.96	-5.79	-0.94	-5.73	-0.92	-5.73	-0.91	-5.79	-0.91	-5.86
3700	4.5	-0.87	-5.67	-0.88	-5.66	-0.88	-5.67	-0.88	-5.74	-0.88	-5.83
3800	4.5	-0.80	-5.52	-0.82	-5.59	-0.83	-5.63	-0.84	-5.69	-0.85	-5.74
3900	4.5	-0.72	-5.40	-0.75	-5.54	-0.79	-5.59	-0.81	-5.65	-0.82	-5.67
4000	4.5	-0.65	-5.28	-0.70	-5.49	-0.74	-5.57	-0.77	-5.61	-0.79	-5.62
4100	4.5	-0.59	-5.21	-0.64	-5.45	-0.68	-5.56	-0.72	-5.58	-0.75	-5.59
4200	4.5	-0.52	-5.22	-0.57	-5.42	-0.63	-5.53	-0.67	-5.57	-0.71	-5.57
4300	4.5	-0.46	-5.18	-0.51	-5.40	-0.56	-5.51	-0.62	-5.55	-0.67	-5.56
4400	4.5	-0.40	-5.17	-0.44	-5.35	-0.50	-5.46	-0.56	-5.52	-0.62	-5.55
4500	4.5	-0.33	-5.11	-0.38	-5.28	-0.43	-5.40	-0.50	-5.48	-0.57	-5.53
4600	4.5	-0.28	-5.06	-0.32	-5.20	-0.37	-5.34	-0.44	-5.43	-0.51	-5.51
4700	4.5	-0.22	-4.95	-0.26	-5.12	-0.31	-5.26	-0.38	-5.37	-0.46	-5.46
4800	4.5	-0.18	-4.92	-0.21	-5.06	-0.27	-5.19	-0.33	-5.30	-0.41	-5.42
4900	4.5	-0.13	-4.85	-0.17	-4.99	-0.22	-5.12	-0.28	-5.22	-0.35	-5.34
5000	4.5	-0.09	-4.78	-0.12	-4.93	-0.17	-5.04	-0.23	-5.15	-0.30	-5.27
5100	4.5	-0.08	-4.62	-0.10	-4.71	-0.14	-4.76	-0.20	-4.77	-0.27	-4.76
5200	4.5	-0.04	-4.57	-0.07	-4.64	-0.10	-4.70	-0.16	-4.72	-0.23	-4.70
5300	4.5	-0.01	-4.55	-0.03	-4.59	-0.06	-4.65	-0.11	-4.66	-0.18	-4.64
5400	4.5	0.02	-4.48	-0.00	-4.55	-0.03	-4.60	-0.10	-4.63	-0.14	-4.59
5500	4.5	0.04	-4.44	0.03	-4.50	0.00	-4.55	-0.04	-4.55	-0.10	-4.54
5600	4.5	0.06	-4.40	0.05	-4.47	0.03	-4.51	-0.01	-4.51	-0.10	-4.52
5700	4.5	0.09	-4.37	0.08	-4.43	0.06	-4.47	0.01	-4.49	-0.06	-4.48
5800	4.5	0.11	-4.34	0.10	-4.40	0.09	-4.44	0.05	-4.45	-0.02	-4.45
5900	4.5	0.14	-4.31	0.12	-4.38	0.10	-4.42	0.07	-4.42	0.01	-4.40
6000	4.5	0.16	-4.28	0.15	-4.35	0.13	-4.38	0.09	-4.39	0.04	-4.37
6100	4.5	0.18	-4.25	0.17	-4.32	0.16	-4.36	0.12	-4.37	0.07	-4.34
6200	4.5	0.20	-4.22	0.19	-4.29	0.18	-4.33	0.14	-4.34	0.09	-4.31
6300	4.5	0.22	-4.19	0.21	-4.26	0.19	-4.31	0.17	-4.31	0.12	-4.29
6400	4.5	0.23	-4.17	0.23	-4.23	0.22	-4.27	0.18	-4.29	0.14	-4.27
6500	4.5	0.24	-4.14	0.24	-4.20	0.23	-4.25	0.21	-4.26	0.16	-4.24
6600	4.5	0.26	-4.11	0.25	-4.17	0.25	-4.22	0.22	-4.24	0.18	-4.22
6700	4.5	0.27	-4.08	0.27	-4.14	0.26	-4.20	0.24	-4.22	0.20	-4.20
6800	4.5	0.28	-4.05	0.28	-4.11	0.28	-4.17	0.26	-4.19	0.22	-4.18
6900	4.5	0.29	-4.02	0.29	-4.08	0.29	-4.14	0.27	-4.17	0.24	-4.16
7000	4.5	0.30	-3.99	0.30	-4.06	0.30	-4.11	0.29	-4.14	0.26	-4.14
7200	4.5	0.31	-3.93	0.32	-4.00	0.32	-4.06	0.31	-4.09	0.28	-4.10
2300	5.0	-3.49	-7.96	-3.23	-7.69	-2.83	-7.36	-2.46	-6.96	-2.21	-6.61
2400	5.0	-3.29	-7.80	-2.99	-7.54	-2.58	-7.19	-2.26	-6.76	-2.04	-6.41
2500	5.0	-3.04	-7.55	-2.68	-7.29	-2.35	-6.93	-2.06	-6.52	-1.88	-6.22
2600	5.0	-2.78	-7.27	-2.41	-7.02	-2.14	-6.67	-1.88	-6.31	-1.73	-6.05
2700	5.0	-2.53	-7.01	-2.25	-6.76	-1.94	-6.46	-1.73	-6.13	-1.59	-5.92
2800	5.0	-2.28	-6.75	-2.03	-6.54	-1.77	-6.25	-1.59	-5.99	-1.47	-5.82
2900	5.0	-2.05	-6.56	-1.83	-6.34	-1.62	-6.09	-1.46	-5.88	-1.36	-5.75
3000	5.0	-1.84	-6.40	-1.65	-6.19	-1.48	-5.97	-1.34	-5.80	-1.25	-5.69
3100	5.0	-1.65	-6.25	-1.50	-6.06	-1.35	-5.88	-1.24	-5.74	-1.16	-5.66
3200	5.0	-1.49	-6.13	-1.37	-5.96	-1.24	-5.81	-1.15	-5.70	-1.09	-5.64
3300	5.0	-1.34	-6.02	-1.25	-5.88	-1.15	-5.76	-1.07	-5.69	-1.02	-5.65
3400	5.0	-1.22	-5.93	-1.15	-5.81	-1.07	-5.73	-1.00	-5.69	-0.97	-5.67
3500	5.0	-1.10	-5.85	-1.05	-5.75	-1.00	-5.69	-0.95	-5.68	-0.92	-5.69
3600	5.0	-1.00	-5.77	-0.97	-5.68	-0.93	-5.63	-0.90	-5.65	-0.88	-5.70
3700	5.0	-0.91	-5.65	-0.90	-5.60	-0.88	-5.57	-0.86	-5.60	-0.85	-5.68
3800	5.0	-0.82	-5.50	-0.82	-5.53	-0.83	-5.52	-0.82	-5.56	-0.82	-5.63
3900	5.0	-0.74	-5.32	-0.76	-5.43	-0.78	-5.48	-0.79	-5.53	-0.79	-5.58
4000	5.0	-0.67	-5.18	-0.69	-5.35	-0.73	-5.44	-0.75	-5.50	-0.76	-5.52
4100	5.0	-0.60	-5.07	-0.64	-5.32	-0.68	-5.41	-0.71	-5.47	-0.73	-5.48

Table D.4. continued.

[Fe/H]		-1.00		-0.50		0.00		+0.50		+1.00	
$T_{\rm eff}$ [K]	$\log g$	log $C_{\rm cf}$	log $R_{\rm HK,\,phot}$	log $C_{\rm cf}$	log $R_{\rm HK,\,phot}$	log $C_{\rm cf}$	log $R_{\rm HK,\,phot}$	log $C_{\rm cf}$	log $R_{\rm HK,\,phot}$	log $C_{\rm cf}$	log $R_{\rm HK,\,phot}$
4200	5.0	-0.54	-5.01	-0.58	-5.27	-0.63	-5.39	-0.67	-5.46	-0.70	-5.45
4300	5.0	-0.47	-5.00	-0.52	-5.24	-0.58	-5.38	-0.63	-5.41	-0.66	-5.42
4400	5.0	-0.42	-4.98	-0.46	-5.23	-0.52	-5.33	-0.58	-5.38	-0.62	-5.41
4500	5.0	-0.36	-4.95	-0.40	-5.13	-0.46	-5.32	-0.52	-5.38	-0.58	-5.40
4600	5.0	-0.30	-4.95	-0.35	-5.14	-0.40	-5.26	-0.46	-5.33	-0.52	-5.38
4700	5.0	-0.25	-4.89	-0.29	-5.07	-0.34	-5.19	-0.40	-5.27	-0.47	-5.34
4800	5.0	-0.20	-4.85	-0.24	-5.00	-0.28	-5.12	-0.35	-5.21	-0.42	-5.29
4900	5.0	-0.15	-4.81	-0.19	-4.94	-0.24	-5.05	-0.29	-5.15	-0.36	-5.24
5000	5.0	-0.11	-4.74	-0.14	-4.88	-0.19	-4.99	-0.25	-5.08	-0.31	-5.18
5100	5.0	-0.09	-4.61	-0.12	-4.70	-0.16	-4.78	-0.22	-4.80	-0.28	-4.79
5200	5.0	-0.06	-4.55	-0.08	-4.64	-0.12	-4.72	-0.17	-4.73	-0.24	-4.73
5300	5.0	-0.03	-4.51	-0.05	-4.59	-0.08	-4.66	-0.13	-4.67	-0.20	-4.68
5400	5.0	0.00	-4.46	-0.02	-4.54	-0.04	-4.60	-0.09	-4.62	-0.15	-4.62
5500	5.0	0.03	-4.43	0.02	-4.50	-0.01	-4.56	-0.06	-4.58	-0.12	-4.57
5600	5.0	0.05	-4.39	0.03	-4.46	0.02	-4.52	-0.04	-4.55	-0.10	-4.55
5700	5.0	0.07	-4.35	0.06	-4.43	0.05	-4.48	-0.01	-4.50	-0.07	-4.49
5800	5.0	0.10	-4.32	0.09	-4.39	0.07	-4.44	0.02	-4.47	-0.04	-4.45
5900	5.0	0.12	-4.29	0.11	-4.36	0.10	-4.41	0.05	-4.43	-0.00	-4.42
6000	5.0	0.14	-4.26	0.13	-4.33	0.12	-4.38	0.08	-4.40	0.03	-4.38
6100	5.0	0.16	-4.24	0.15	-4.30	0.14	-4.35	0.10	-4.36	0.06	-4.35
6200	5.0	0.18	-4.21	0.18	-4.27	0.16	-4.33	0.13	-4.34	0.08	-4.33
6300	5.0	0.20	-4.18	0.19	-4.25	0.18	-4.29	0.15	-4.31	0.10	-4.30
6400	5.0	0.21	-4.16	0.21	-4.23	0.20	-4.27	0.17	-4.29	0.13	-4.27
6500	5.0	0.23	-4.13	0.23	-4.20	0.22	-4.25	0.19	-4.27	0.15	-4.25
6600	5.0	0.24	-4.12	0.24	-4.17	0.23	-4.22	0.21	-4.24	0.17	-4.23
6700	5.0	0.25	-4.09	0.25	-4.15	0.25	-4.20	0.23	-4.22	0.19	-4.21
6800	5.0	0.26	-4.07	0.26	-4.12	0.26	-4.17	0.24	-4.20	0.21	-4.19
6900	5.0	0.27	-4.04	0.28	-4.10	0.27	-4.15	0.26	-4.18	0.23	-4.17
7000	5.0	0.28	-4.02	0.28	-4.07	0.29	-4.12	0.27	-4.16	0.24	-4.15
7200	5.0	0.30	-3.97	0.30	-4.02	0.30	-4.07	0.30	-4.11	0.27	-4.11

Table D.5. Chi values of PHOENIX model atmospheres

$T_{\rm eff}$ [K]	[Fe/H]	$\chi_{\rm CaIIHK}$ $\times 10^{-4}$	$\chi_{\rm H\alpha}$ $\times 10^{-4}$
2300	-1.0	0.000551	0.202107
2400	-1.0	0.000788	0.192654
2500	-1.0	0.001321	0.257018
2600	-1.0	0.002428	0.374069
2700	-1.0	0.004713	0.573781
2800	-1.0	0.009718	0.857325
2900	-1.0	0.018792	1.180935
3000	-1.0	0.034808	1.526253
3100	-1.0	0.060607	1.872651
3200	-1.0	0.096861	2.212708
3300	-1.0	0.143898	2.551446
3400	-1.0	0.200437	2.881837
3500	-1.0	0.266487	3.204793
3600	-1.0	0.344311	3.524350
3700	-1.0	0.437417	3.839320
3800	-1.0	0.549425	4.150202
3900	-1.0	0.683523	4.462624
4000	-1.0	0.827883	4.754775
4100	-1.0	0.987884	5.042933
4200	-1.0	1.146199	5.301651
4300	-1.0	1.322262	5.590931
2300	-0.5	0.000998	0.171112
2400	-0.5	0.001491	0.157325
2500	-0.5	0.002967	0.216378
2600	-0.5	0.005836	0.330543
2700	-0.5	0.009153	0.403176
2800	-0.5	0.017915	0.628417
2900	-0.5	0.034500	0.940191
3000	-0.5	0.059440	1.295086
3100	-0.5	0.094095	1.678432
3200	-0.5	0.137106	2.056224
3300	-0.5	0.187938	2.429038
3400	-0.5	0.244146	2.784152
3500	-0.5	0.306810	3.129856
3600	-0.5	0.375939	3.460377
3700	-0.5	0.452755	3.778883
3800	-0.5	0.542023	4.091369
3900	-0.5	0.638553	4.381635
4000	-0.5	0.750407	4.663454
4100	-0.5	0.869224	4.931749
4200	-0.5	0.993874	5.173299
4300	-0.0	1.141496	5.448736
2300	0.0	0.002397	0.188068
2400	0.0	0.003729	0.203213
2500	0.0	0.006476	0.186438
2600	0.0	0.011695	0.244792
2700	0.0	0.021565	0.362157
2800	0.0	0.038689	0.555819
2900	0.0	0.064316	0.808300
3000	0.0	0.099613	1.106536
3100	0.0	0.141954	1.432723
3200	0.0	0.191728	1.779128
3300	0.0	0.245980	2.132738
3400	0.0	0.300718	2.478126
3500	0.0	0.356153	2.833188
3600	0.0	0.411375	3.182271
3700	0.0	0.467986	3.522503
3800	0.0	0.526894	3.854023
3900	0.0	0.591553	4.162256

Table D.5. continued.

$T_{\rm eff}$ [K]	[Fe/H]	$\chi_{\rm CaIIHK}$ $\times 10^{-4}$	$\chi_{\rm H\alpha}$ $\times 10^{-4}$
4000	0.0	0.661128	4.451381
4100	0.0	0.739789	4.728403
4200	0.0	0.826032	4.978128
4300	0.0	0.933288	5.260589
2300	+0.5	0.006413	0.238301
2400	+0.5	0.010061	0.260112
2500	+0.5	0.016492	0.247500
2600	+0.5	0.027800	0.292038
2700	+0.5	0.044263	0.407142
2800	+0.5	0.068607	0.575496
2900	+0.5	0.102022	0.786998
3000	+0.5	0.143249	1.020113
3100	+0.5	0.191720	1.265885
3200	+0.5	0.244465	1.513235
3300	+0.5	0.298218	1.760222
3400	+0.5	0.349878	2.011364
3500	+0.5	0.397360	2.282790
3600	+0.5	0.439667	2.586420
3700	+0.5	0.478450	2.923161
3800	+0.5	0.514756	3.277294
3900	+0.5	0.550537	3.628710
4000	+0.5	0.588930	3.979705
4100	+0.5	0.639626	4.358765
4200	+0.5	0.700250	4.708474
4300	+0.5	0.782585	5.064212
2300	+1.0	0.014411	0.333220
2400	+1.0	0.021711	0.338989
2500	+1.0	0.032464	0.340200
2600	+1.0	0.048820	0.374320
2700	+1.0	0.070960	0.481655
2800	+1.0	0.100049	0.628507
2900	+1.0	0.136855	0.803741
3000	+1.0	0.180487	0.983418
3100	+1.0	0.229947	1.156046
3200	+1.0	0.280350	1.308436
3300	+1.0	0.329080	1.442195
3400	+1.0	0.372528	1.561571
3500	+1.0	0.410402	1.683466
3600	+1.0	0.443302	1.836109
3700	+1.0	0.470929	2.065178
3800	+1.0	0.497274	2.413894
3900	+1.0	0.529802	2.873790
4000	+1.0	0.564174	3.366484
4100	+1.0	0.601777	3.868406
4200	+1.0	0.655195	4.370432
4300	+1.0	0.718588	4.824441